OULU 2014
C 495

ACTA UNIVERSITATIS OULUENSIS

Saara Mehtonen

THE BEHAVIOR OF STABILIZED HIGH-CHROMIUM FERRITIC STAINLESS STEELS IN HOT DEFORMATION

UNIVERSITY OF OULU GRADUATE SCHOOL;
UNIVERSITY OF OULU,
FACULTY OF TECHNOLOGY,
MECHANICAL ENGINEERING

ACTA UNIVERSITATIS OULUENSIS
C Technica 495

SAARA MEHTONEN

THE BEHAVIOR OF STABILIZED HIGH-CHROMIUM FERRITIC STAINLESS STEELS IN HOT DEFORMATION

Academic dissertation to be presented with the assent of the Doctoral Training Committee of Technology and Natural Sciences of the University of Oulu for public defence in the OP auditorium (L10), Linnanmaa, on 8 August 2014, at 12 noon

UNIVERSITY OF OULU, OULU 2014

Acta Univ. Oul. C 495, 2014

Supervised by
Professor David Porter

Reviewed by
Professor Matthew Barnett
Professor Beatriz López

Opponent
Professor Bevis Hutchinson

ISBN 978-952-62-0493-2 (Paperback)
ISBN 978-952-62-0494-9 (PDF)

ISSN 0355-3213 (Printed)
ISSN 1796-2226 (Online)

Cover Design
Raimo Ahonen

JUVENES PRINT
TAMPERE 2014

Mehtonen, Saara, The behavior of stabilized high-chromium ferritic stainless steels in hot deformation.
University of Oulu Graduate School; University of Oulu, Faculty of Technology, Mechanical Engineering
Acta Univ. Oul. C 495, 2014
University of Oulu, P.O. Box 8000, FI-90014 University of Oulu, Finland

Abstract

In this thesis, the hot deformation behavior of stabilized 12–27% Cr ferritic stainless steels was investigated in order to find ways to improve the current hot rolling schedules for enhancing texture structures and deep drawability of the end product. Hot deformation was studied using axial and plane strain compression in two thermomechanical simulators: a Gleeble and a TMC machine. In addition to flow stress measurements, the resultant microstructures and textures were investigated using electron backscatter diffraction (EBSD), and the dislocation structures using transmission electron microscopy (TEM). In the case of 21% Cr steel, industrial multi-pass hot rolling, including low finish rolling temperatures, was simulated in order to investigate the microstructure and texture development under varying deformation conditions.

Flow behavior of high-Cr ferritic stainless steels during hot deformation was mainly controlled by intense dynamic recovery. However, the deformation conditions greatly affected the extent of dynamic recovery. Cr increased the flow stress through solid solution hardening, although increasing the Cr content reduced the activation energy for hot deformation. Two modeling approaches for flow stress were successfully applied: an empirical constitutive equation and a dislocation density-based flow stress model. Continuous dynamic recrystallization was identified regardless of the Zener-Hollomon parameter, whereas discontinuous dynamic recrystallization was not observed. Static recrystallization slowed down towards the completion of the process, and especially the α fiber grains were difficult to recrystallize. Static recrystallization was enhanced by lowering the deformation temperature to 800 °C or below due to the accelerating effect of in-grain shear bands on the static recrystallization kinetics. However, an intensifying effect on γ fiber texture development was achieved after deformation at 600 °C or below.

Two different improved process routes for hot rolling were proposed based on the results: 1) sufficiently long inter-pass times together with lowering the finish rolling temperature in order to promote static recrystallization during inter-pass times and hot band annealing, and 2) hot band annealing preceded by a warm rolling procedure, in which thin gauge hot band is produced by multiple heavy warm rolling deformation passes.

Keywords: ferritic stainless steel, flow stress, hot deformation, recrystallization, texture

Mehtonen, Saara, Stabiloitujen korkeakromisten ferriittisten ruostumattomien terästen kuumamuokkauksen aikaiset ilmiöt.
Oulun yliopiston tutkijakoulu; Oulun yliopisto, Teknillinen tiedekunta, Konetekniikka
Acta Univ. Oul. C 495, 2014
Oulun yliopisto, PL 8000, 90014 Oulun yliopisto

Tiivistelmä

Tässä väitöstyössä tutkittiin stabiloitujen 12–27 % kromia sisältävien ferriittisten ruostumattomien terästen käyttäytymistä kuumamuokkauksessa tavoitteena kehittää nykyisin käytössä olevia kuumamuokkauskäytäntöjä lopputuotteen tekstuurirakenteen ja siten sen syvävedettävyyden parantamiseksi. Kuumamuokkausta simuloitiin sylinteri- ja tasomuodonmuutospuristuskokeilla Gleeble- ja TMC-laitteistoissa. Kokeista saatuja jännitys–venymä-käyriä analysoitiin ja syntyneet mikrorakenteet ja tekstuuri tutkittiin EBSD-menetelmällä pyyhkäisyelektronimikroskoopissa sekä dislokaatio- ja erkaumarakenteet läpäisyelektronimikroskoopilla. Lisäksi 21 % kromia sisältävälle teräkselle tehtiin monipistoista kuumavalssausta simuloivia puristuskokeita, joissa varioitiin myös valssauksen lopetuslämpötilaa ja jäähtymisnopeutta.

Jännitys–venymä-käyriä mallinnettiin käyttäen sekä empiirisiä yhtälöitä että dislokaatiotiheyteen perustuvaa fysikaalista mallia. Kromipitoisuus kasvatti muodonmuutosvastusta mutta pienensi deformaation aktivaatioenergiaa. Dynaaminen toipuminen oli erittäin voimakasta kuumamuokkauslämpötiloissa, joskin lämpötila ja muodonmuutosnopeus vaikuttivat merkittävästi sen määrään. Jatkuvan dynaamisen rekristallisaation todettiin tapahtuvan riippumatta Zener-Hollomon -parametrin arvosta, mutta epäjatkuvaa dynaamista rekristallisaatiota ei havaittu. Staattinen rekristallisaatio hidastui, kun rekristallisaatioaste saavutti 90 %, ja erityisesti α-rungon rakeet pyrkivät vain toipumaan. Staattista rekristallisaatiota pystyttiin voimistamaan laskemalla muokkauslämpötila 800 °C:een tai sen alle, jolloin rakeiden sisälle syntyi staattisen rekristallisaation ydintymistä nopeuttavia leikkausnauhoja. γ-rungon intensiteetti voimistui rekristallisaatiossa kuitenkin vasta, kun muokkauslämpötila oli 600 °C tai tätä matalampi.

Koetulosten perusteella ehdotettiin kahta erilaista kuumavalssauspraktiikkaa, joiden avulla kuumanauhan ominaisuuksia voidaan parantaa: 1) staattisen rekristallisaation edistäminen sekä pistojen välillä että kuumanauhahehkutuksessa käyttämällä pitkiä pistojen välisiä aikoja sekä laskemalla valssauksen lopetuslämpötilaa, tai 2) kuumanauhahehkutus yhdistettynä edeltävään voimakkaaseen lämminvalssaukseen, jolloin on mahdollista valmistaa ohutta kuumanauhaa.

Asiasanat: ferriittinen ruostumaton teräs, kuumamuokkaus, puristuskoe, rekristallisaatio, tekstuuri, toipuminen

Ancora imparo

-Michelangelo

Acknowledgements

This thesis contains work carried out during 2010–2013 at the Materials Engineering Laboratory of the Centre for Advanced Steels Research (CASR) at the University of Oulu. The research was funded by the Academy of Finland through the national Graduate School on Advanced Materials and Processes, and by the Finnish Funding Agency for Technology and Innovation (Tekes) under the CSP1 project of the Demanding Applications program of the Finnish Metals and Engineering Competence Cluster (FIMECC Ltd). The experimental materials were provided by Outokumpu Oyj. This thesis has also been supported by scholarships awarded by Tekniikan Edistämissäätiö (TES) and KAUTE foundation.

During this 4-year process, I have received guidance and support from several experts and other people, to whom I am extremely grateful and whose contribution I would like to acknowledge. Firstly, I would like to thank my supervisors Professor David Porter and Professor Emeritus Pentti Karjalainen for their guidance and valuable comments on my research papers and on this thesis.

Dr. Eric Palmiere is to be acknowledged for supervising my experimental work during my visit to the University of Sheffield, and for the valuable comments on my research papers based on the experimental work carried out during my research visit. I also wish to thank Professor Devesh Misra from the University of Louisiana at Lafayette for performing the TEM examinations and contributing to the two journal articles. I would also like to express my gratitude to Professor Matthew Barnett from Deakin University and Professor Beatriz López from CEIT and Tecnun, Universidad de Navarra, for the pre-examination of this thesis and for the suggestions for improving the manuscript.

Furthermore, I would like to thank my colleagues at the Materials Engineering Laboratory and elsewhere who have in one way or another been involved in this process. I want to give special thanks to Miss Anna Kisko for invaluable peer-support and for providing unforgettable adventures inside and outside office hours.

Finally, I would like to thank my family and friends, especially my parents and Mikko, for their support and encouragement during these years.

Oulu, May 2014 Saara Mehtonen

Symbols and abbreviations

a	Stress multiplier, a material constant
A	Material constant
A_1	Material constant
b	Burger's vector
B	Constant
c	Power law exponent
C	Material constant
$C_{0.5}$	Material constant
d	Grain size (μm)
D_{eff}	Effective diffusion coefficient
D_v	Lattice diffusion coefficient
G	Shear modulus (GPa)
n	Avrami exponent
n_c	Material constant
p	Strain exponent, material constant
Q_{app}	The apparent activation energy for static recrystallization (kJ/mol)
Q_{cr}	Activation energy for creep (kJ/mol)
Q_{def}	Activation energy for deformation (kJ/mol)
Q_{diff}	Activation energy for self-diffusion (kJ/mol)
Q_m	Activation energy for vacancy diffusion (kJ/mol)
q	Strain rate exponent, material constant
r	Lankford coefficient
R	Universal gas constant (8.3145 kJ/mol)
s	Grain size exponent, material constant
t	Time (s)
$t_{0.5}$	Time for 50% of recrystallization (s)
T	Temperature (K)
T_m	Melting point (K)
U	Work hardening parameter (m^{-2})
$\overline{v}$	Average velocity of mobile dislocations (m/s)
v_c	Velocity of a climbing edge dislocation (m/s)
V	Atomic or ionic volume (m^3)
Z	Zener-Hollomon parameter (s^{-1})
Z'	Modified Zener-Hollomon parameter (s^{-1})
Z''	Further modified Zener-Hollomon parameter (s^{-1})

X_{rex}	Statically recrystallized fraction
α	Ferrite
γ	Taylor constant
Δr	Planar anisotropy
ε	True strain
ε'	Strain rate (s^{-1})
Ω	Recovery parameter
ρ	Dislocation density (m^{-2})
ρ_m	Density of mobile dislocations (m^{-2})
ρ_{ss}	Dislocation density during steady state flow (m^{-2})
ρ_0	Initial dislocation density (m^{-2})
σ	True stress (MPa)
σ_0	Initial stress (MPa)
σ_n	Local normal stress (MPa)
σ_p	Peak stress (MPa)
σ_s	Shear stress (MPa)
σ_{ss}	Steady state stress (MPa)
BCC	Body centered cubic
CDRX	Continuous dynamic recrystallization
CSL	Coincident site lattice
DDRX	Discontinuous dynamic recrystallization
DRV	Dynamic recovery
DRX	Dynamic recrystallization
DSA	Dynamic strain ageing
EBSD	Electron backscatter diffraction
FEG-SEM	Field emission gun scanning electron microscope
HAGB	High-angle grain boundary
IF	Interstitial free
LAGB	Low-angle grain boundary
ND	Normal direction
ODF	Orientation distribution function
PSN	Particle stimulated nucleation
RD	Rolling direction
SFE	Stacking fault energy
SRV	Static recovery

SRX	Static recrystallization
TD	Transverse direction
TEM	Transmission electron microscope
TMC	Thermomechanical compression machine

List of original publications

This thesis is based on the following publications, which are referred to in the text by their Roman numerals (I–V):

I Mehtonen S, Karjalainen P & Porter D (2014) Modeling of the high temperature flow behavior of stabilized 12–27 wt% Cr ferritic stainless steels. Materials Science & Engineering A 607: 44–52.

II Mehtonen S, Karjalainen P & Porter D (2013) Hot deformation behavior and microstructure evolution of a stabilized high-Cr ferritic stainless steel. Materials Science & Engineering A 571: 1–12.

III Mehtonen S, Palmiere E, Misra D, Karjalainen P & Porter D (2014) Dynamic restoration mechanisms in a Ti-Nb stabilized ferritic stainless steel during hot deformation. Materials Science & Engineering A 601: 7–19.

IV Mehtonen S, Palmiere E, Misra D, Karjalainen P & Porter D (2014) Microstructural and texture development during multi-pass hot deformation of a stabilized high-chromium ferritic stainless steel. ISIJ International 54(6): 1406–1415.

V Mehtonen S, Karjalainen P & Porter D (2013) Effect of hot deformation temperature on the restoration mechanisms and texture in a high-Cr ferritic stainless steel. Materials Science Forum 762: 705–710.

Saara Mehtonen has been the main and corresponding author of all the publications. She has planned the tests, performed all the experiments, except for the Gleeble compression tests for Papers I, II and V, and the TEM examinations for Papers III and IV, and carried out the data analysis.

Paper I concerns ferritic stainless steels containing 12–27% Cr. It describes the flow behavior and the development of a flow stress model, which is a combination of physical and empirical equations, and which successfully predicts the flow stress for ferritic stainless steels with various Cr contents.

In Paper II, a phenomenological flow stress model for 21% Cr ferritic stainless steel is developed. The effect of strain is incorporated in the model. Further, the dynamic and static microstructure evolution during and after hot deformation is presented together with static recrystallization kinetics.

Paper III focuses on the dynamic microstructure and texture evolution under various laboratory deformation conditions. The dynamic restoration mechanisms under different deformation conditions were identified as well as their effect on the texture formation and dislocation structures.

In paper IV, the behavior of a high-Cr ferritic stainless steel in multi-pass hot deformation is described, and the effect of the final pass temperature on

microstructure, texture and dislocation structure was investigated. The process parameters were relevant to industrial Steckel mill rolling.

Paper V focuses on the effect of deformation temperature on the deformed microstructure and texture, and on the static recrystallization kinetics and texture development during subsequent annealing. The deformation temperature range from 550 °C to 950 °C was employed. Also the possibility of utilizing warm deformation in the production of high-Cr ferritic stainless steels is discussed.

Table of contents

1 Introduction

1.1 High-Cr ferritic stainless steels and their applications

The dual Ti-Nb stabilized ferritic stainless steels, which contain over 20% Cr, are a rather new and very promising steel group. They are Fe-Cr alloys, which contain very low concentrations Ni and Mo, usually less than 1%. However, due to their high Cr content, stabilization, and alloying with Cu, the corrosion resistance of these ferritic grades is comparable to that of the commonly used austenitic grade AISI 304 but with much lower alloying costs [1].

Typical applications for these high-Cr ferritic stainless steels include kitchen appliances, electrical equipment, and building materials for general indoor and outdoor applications. In fact, in these applications the high-Cr ferritic grades are designed to replace the commonly used austenitic grades. The key requirement for these applications is good formability, especially deep drawability. Factors needed for good deep drawability are resistance to ridging e.g. [2], high normal anisotropy, which is presented using the Lankford coefficient (r) e.g. [3, 4], and low planar anisotropy (Δr).

1.2 The deep drawability of ferritic stainless steels

Although the high Cr content itself is known to increase the r-value [3, 4], the ferritic stainless steels may develop unfavorable texture structures and are, therefore, prone to ridging, which is caused by heterogeneities in the texture structure and differences in the plastic anisotropies of grains [2]. Ridging defects appear as corrugations parallel to the rolling direction of the sheet after the deep drawing process, and their occurrence ruins the product's appearance.

The solidification structure of ferritic stainless steels consists of columnar grains, which are transformed during recrystallization into bands or colonies of similarly oriented grains, which may remain in the microstructure to the final product. Ridging occurs because these grain colonies have different plastic anisotropies compared to the matrix [2]. It has been shown in [5, 6] that breaking up these colonies of similarly oriented grains in the cold rolled and annealed sheet can prevent ridging during deep drawing. The texture of final cold rolled and annealed sheet is, however, inherited from the hot band [7, 8] and, since austenite–ferrite phase transformation does not occur in these ferritic grades,

recrystallization during hot rolling and/or hot band annealing is the only way to weaken the unfavorable texture structures in the course of hot deformation.

The r-value, which also affects deep drawability, is closely related to the intensity of the γ fiber (<111>//ND) texture in ferritic stainless steels e.g. [3, 4] and therefore, in order to improve the deep drawability, the formation of the γ fiber texture should be promoted. Since the γ fiber grains are formed often during static recrystallization (SRX), SRX during annealing stages after hot and cold rolling should be promoted. If SRX is not fully completed during the post-cold rolling annealing, the r-value is likely to be decreased due to the remaining unrecrystallized α fiber (<110>//RD) grains [9].

1.3 Why investigate hot deformation?

In order to achieve good final product properties, affecting the texture structures already in the hot rolling stage is very important. Especially due to the tendency of ferritic stainless steels to develop α fiber textures in hot rolled sheets e.g. [7, 8]. The hot band textures might even sharpen slightly during the cold rolling, and it is therefore beneficial to increase the amount of γ fiber texture already in the hot rolled and annealed sheet.

After deformation passes SRX plays a key role in achieving a favorable texture. However, dynamic recovery (DRV), which is very extensive in ferritic stainless steels at conventional hot deformation temperatures due to the high stacking fault energy (SFE), reduces the amount of stored energy in the microstructure and therefore also the driving force for SRX. If SRX does not fully proceed through the microstructure during the inter-pass times or hot band annealing, positive texture development may not be achieved and ridging defects may appear in deep drawing.

The majority of all steels are austenitic at high hot deformation temperatures, and therefore the hot deformation studies have been mostly carried out on austenite, while much less attention has been paid to the hot deformation behavior of ferrite at high temperatures. Austenite and ferrite behave differently during hot deformation due to their different SFEs. Furthermore, the phase transformation from austenite to ferrite offers an additional way to refine the grain size and affect the texture formation for most of the steels, but not for stabilized high-Cr ferritic stainless steels.

Glover and Sellars [10, 11] investigated the flow behavior, dynamic restoration mechanisms and static recrystallization of α-iron as early as in the

1970's. However, their experiments were carried out in the ferritic temperature range, i.e. below 850 °C. Hinton and Beynon [12] simulated Steckel mill hot rolling on ferritic AISI 430; however, the AISI 430 grade undergoes a phase transformation, which affects the restoration mechanisms and texture development. Recently, Gao et al [13, 14] and Zhang *et al.* [15] published investigations into the hot deformation of 17% Cr and 21% Cr ferritic stainless steels; however, they focused solely on the effect of lowering the hot rolling finishing temperature and neglected many of the important features of hot deformation, e.g. the flow stress. Gao *et al.* [16] investigated the dynamic microstructure evolution of 26% Cr ferritic stainless steel in hot deformation. However, they employed very few laboratory deformation conditions and neglected the texture development. SRX kinetics, and the correlation between SRX structures and deep drawability of a stabilized ferritic stainless steel have been investigated in detail by Sinclair *et al.* [9, 17–19] although they only investigated the SRX after cold deformation, not after hot deformation.

On the other hand, there are a great number of studies on warm rolling, i.e. rolling in the ferritic state, of various carbon and IF steels e.g. [20–25]. However, all those investigations take place at a rather low temperature and not in high hot rolling temperatures, and it can be expected that the restoration mechanisms differ significantly from each other at those two different temperatures.

These previous investigations cover narrow and separate areas of hot or warm deformation behavior of various ferritic steels, and a comprehensive investigation, which would bring all the pieces of the puzzle together, has yet to be carried out.

1.4 Aims of this study

The objective of this thesis is to acquire from different aspects of hot deformation an understanding of stabilized high-Cr ferritic stainless steels in order to enable the optimization of the hot rolling parameters and to achieve enhanced deep drawability of the end product. The different aspects of hot deformation that are covered in the current investigation and the scope of the thesis are presented in Fig. 1.

The investigations into flow behavior include describing the flow behavior of high-Cr ferritic stainless steel under various deformation conditions and flow stress modeling using either empirical constitutive equations or physical equations, e.g. Bergström's model. The dynamically and statically formed microstructures will be investigated in order to identify the restoration

mechanisms and their effect on microstructure and texture evolution. Also, the behavior of stabilized high-Cr ferritic stainless steel in conventional Steckel mill rolling will be investigated by performing Steckel mill rolling simulations.

By combining the information from all of these different aspects of hot deformation, new knowledge will be acquired on the hot deformation behavior of ferritic stainless steels. Using the new knowledge for improving the industrial hot rolling processing order in order to enhance the final product properties is the main goal of this thesis. The objective of this work can be divided into the following tasks:

- To investigate the flow behavior of high-Cr ferritic stainless steels and to develop flow stress models that can accurately predict the flow stress under various deformation conditions.
- To study the deformation microstructures, textures and dislocation structures formed under various deformation conditions.
- To study the dynamic and static restoration mechanisms and their kinetics during hot deformation and subsequent annealing, and to define how the hot deformation conditions and grain orientation affect these.
- To find ways to improve conventional hot rolling schedules in order to achieve better deep drawability of the end product.

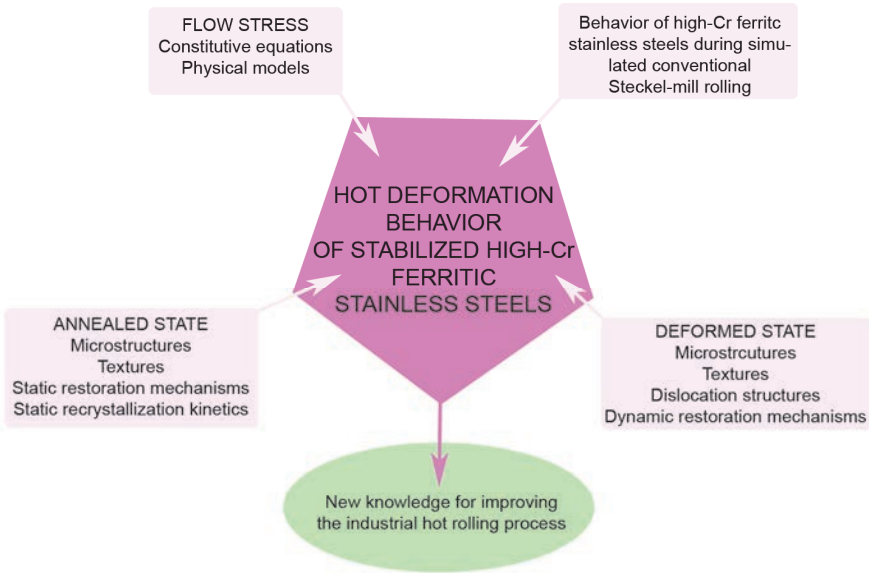

Fig. 1. The scope of the thesis.

2 Theory of hot deformation

2.1 Deformation mechanisms

2.1.1 Low temperature plasticity

Deformation in metal crystals occurs through the movement of dislocations along a slip plane. At low temperatures the movement occurs through glide, which, however, is often hindered by various obstacles e.g. interactions with other mobile or immobile dislocations, with solute atoms or precipitates, or with grain boundaries. The velocity of mobile dislocations depends on the force on the dislocation and on its mobility. The average velocity of mobile dislocations that are moving through various obstacles is determined almost completely by their waiting time at obstacles. Therefore, the strain rate can be written as follows [26]:

$$\dot{\varepsilon} = \rho_m b \bar{v}, \tag{1}$$

where $\dot{\varepsilon}$ is the strain rate, ρ_m the density of mobile dislocations, b the magnitude of the Burger's vector and $\bar{v}$ the average velocity of the mobile dislocations. During steady state deformation, ρ_m is a function of temperature and stress, and can be expressed as follows:

$$\rho_m = B\left(\frac{\sigma_s}{Gb}\right)^2, \tag{2}$$

where B is a constant of order unity, σ_s the shear stress, G the shear modulus, and b the length of the Burger's vector [26].

The crystal lattice presents an array of barriers to the motion of the dislocation, which naturally fluctuates with its position [26]. The interaction of the dislocation with the atomic structure of the material is referred to as *lattice resistance* or *Peierls-Nabarro stress*, which describes the amount of shear stress needed to move a dislocation on a slip plane from one equilibrium position to the next [27]. The scale of the Peierls-Nabarro force depends on the inter-planar spacing, which is the smallest with close-packed planes where the Burger's vector of a dislocation is also the shortest. Therefore, dislocations tend to move on the closest packed planes [27].

Due to the lattice resistance, the dislocations move forward by kink pairs, which can be assisted mechanically or thermally. Therefore, under external

pressure and/or at high temperatures, the movement of dislocations gets easier. The limiting factor for dislocation velocity is the nucleation rate of kink pairs. The required activation energy for the nucleation of the kink pairs depends on the way in which the dislocation energy fluctuates with distance and on the temperature and applied stress. [26]

Therefore, at low temperatures and in the absence of discrete obstacles to dislocation movement, the strain rate under a constant load is dependent on the lattice resistance, i.e. the Peierls-Nabarro stress, and therefore on the kinetics of kink nucleation and the propagation of kink pairs. However, if there are discrete obstacles to dislocation movement on the slip plane, e.g. precipitates, the strain rate is then dependent on the ability of dislocations to pass the obstacles [26]. Hard precipitates impose a great effect on the moving dislocations, which can also been seen as an increase in the flow stress [26]. The effect of finely dispersed less hard precipitates differs from that of the hard particles, since the soft particles can be cut by the moving dislocations. However, if the density of the soft particles is high enough, they will effectively increase the resistance to dislocation movement, i.e. the flow stress [26].

Also, solute atoms can increase the strength by various mechanisms, e.g. segregation to dislocations and can therefore cause Cottrell locking, producing elastic interactions of solute atoms with moving dislocations, i.e. increasing Peierls-Nabarro stress or friction stress, by segregating to stacking faults (i.e. Suzuki interactions), or by interacting with dislocation jogs and vacancies. However, the effect of solute atoms is less than that of hard precipitates. [27]

2.1.2 Creep

At high temperatures, i.e. at or above $0.3T_m$ for pure metals and $0.4T_m$ for alloys, metals show rate-dependent plasticity, which is referred to as creep. The deformation becomes highly dependent on the strain rate, and it can be expressed by a *power law*, which can be written as follows [26]:

$$\dot{\varepsilon} \propto \left(\frac{\sigma_s}{G} \right)^c , \tag{3}$$

where $\dot{\varepsilon}$ is the strain rate, σ_s the shear stress, G the shear modulus, and c the power law exponent. [26]

Creep can occur though glide alone, or it can be assisted by climb of dislocations at high temperatures. The mechanism depends on the temperature, and the operating mechanism affects the exponent c in the power law (Eq. 3). By climbing, the moving dislocation can overcome obstacles on the slip plane. The mechanism is often referred to as *climb-controlled creep*, in which the rate-controlling mechanism at the atomic level is the diffusion of single ions or vacancies to and from the moving dislocation, and not the activation energy of the glide of the dislocation. Therefore, at temperatures of $0.6T_m$ or above, climb of dislocations is controlled by lattice diffusion.

The velocity of a climbing edge dislocation can be expressed using the following equation:

$$v_c \approx \frac{D_v \sigma_n V}{bRT}, \tag{4}$$

where D_v is the lattice diffusion coefficient, σ_n the local normal stress, V the atomic or ionic volume, b the length of the Burger's vector, R the universal gas constant (8.3145 kJ/mol), and T the temperature. By combining Eqs. 1 and 2, by approximating V in Eq. 4 by b^3 and by adding a dimensionless constant A_1, the strain rate (Eq. 3) can be written as [26]:

$$\dot{\varepsilon} = A_1 \frac{D_{eff} Gb}{RT} \left(\frac{\sigma_s}{G} \right)^c, \tag{5}$$

where A_1 is a constant, D_{eff}, the effective diffusion coefficient, G the shear modulus, b the length of the Burger's vector, R the gas constant (8.3145 kJ/mol), T the temperature, σ_s the shear stress, and c the power law exponent. The Eq. 5 actually combines two equations depending on which type of diffusion is dominant – the difference is visible in the diffusion coefficient D_{eff}. At high temperatures lattice diffusion occurs and can often be stress-directed, in which case, the creep mechanism is referred to as Nabarro-Herring creep [27]. At lower temperatures where core/grain boundary diffusion controls creep, the creep mechanism is called Coble creep [26].

At high stresses, i.e. at low temperatures, the calculated strain rate values using Eq. 5 are systematically lower than the actual measured ones, and the power law does not apply. The phenomenon is referred to as *power law bread-down*, and the main cause for it is the change in the dominant creep mechanism from climb to glide, which then controls the flow. Creep through glide of dislocations cannot

be described using entirely physical equations, and therefore different empirical equations have been suggested, e.g. the following equation: [26]

$$\dot{\varepsilon} \propto \exp(a\sigma_s)\exp-\left(\frac{Q_{cr}}{RT}\right), \tag{6}$$

where a is a dimensionless constant and a stress multiplier, σ_s is the shear stress and Q_{cr} the activation energy for creep.

Sellars and Tegart [28] introduced a generalization of Eq. 6:

$$\dot{\varepsilon} \propto \left[\sinh(a\sigma_s)\right]^c \exp-\left(\frac{Q_{cr}}{RT}\right), \tag{7}$$

which is referred to as the hyperbolic sine equation. At low stresses ($a\sigma_s < 0.8$) Eq. 7 becomes a power law (Eq. 5) and at high stresses ($a\sigma_s > 1.2$) an exponential equation [26].

The activation energy for creep, Q_{cr}, derived from the above equations 6 or 7 can then be used for distinguishing between the possible creep mechanisms. However, in the power law break-down region, the calculated Q_{cr} values tend to be significantly larger than that of self-diffusion. The difference can be taken as an indication of a change in the creep mechanisms. However, it may also just be a result of the temperature dependency of the shear modulus, which becomes more significant in the exponential region, i.e. at high stresses [26].

The two mechanisms associated with creep have so far been climb and glide. However, cross-slip of screw dislocations, i.e. movement of screw dislocations to another slip plane of the same direction, can also occur at intermediate temperatures in high SFE metals, e.g. at $0.6–0.9T_m$ for Al. Cross-slip enables screw dislocations to pass obstacles on their current slip plane, and therefore the occurrence of cross-slip reduces the Q_{cr}. Cross-slip does not require diffusion of vacancies, however the mechanism is thermally activated [27].

2.1.3 Hot deformation

During hot deformation, the deformation behavior is strongly affected by the interaction of the dislocations with crystal defects: vacancies enable the climb of dislocations at high temperatures and cross-slip of screw dislocations is thermally activated [29]. The equations developed for creep for predicting extensions under specific loads (Eqs. 6 and 7) can also be employed for hot deformation for calculating the loads under constant strain rates [30]. Unlike in creep, where the

load is kept constant, in hot deformation the strain rate is constant. However, a common feature of both is that the temperature is elevated and kept constant. The main difference, however, is in the magnitude of the strain rate. Due to the high strain rates in hot deformation, the power law breaks down and therefore cannot be employed for flow stress calculations. However, the hyperbolic sine equation (Eq. 7) can be employed for the whole stress range in hot deformation. [26]

The hyperbolic sine equation is often presented with the Zener-Hollomon parameter (Z). Z combines the effect of strain rate and deformation temperature into one parameter and is also referred to as the temperature-compensated strain rate. Z is defined as follows:

$$Z = \dot{\varepsilon}\exp\left(\frac{Q_{def}}{RT}\right) = A\left[\sinh\left(a\sigma\right)\right]^{n_c}, \tag{8}$$

where $\dot{\varepsilon}$ is the strain rate, Q_{def} is the activation energy of deformation, R the gas constant (8.3145 kJ/mol), T the deformation temperature (K), A a material constant, and a a stress multiplier and an adjustable constant, which brings $a\sigma$ into the right range while σ represents the true stress [31]. The method for determining the variables in Eq. 8 is explained in Paper II.

Eq. 8 can also be employed for calculating the activation energy for hot deformation. Generally, the Q_{def} gives information about the difficulty of the atomic rearrangements involved in the rate-controlling mechanism [32] and therefore, the calculated activation energy can be compared to the activation energies of various physical phenomena in order to identify the operating mechanisms. For instance, when the hot deformation is controlled by climb of dislocations assisted by diffusing vacancies, which has been observed to be the case for pure metals, the activation energy of hot deformation is equal or very close to that of self-diffusion [33]. However, for two-phase materials, the Q_{def} values can be significantly higher than that of self-diffusion [33].

When the rate controlling mechanisms of hot deformation is sub-grain formation by dislocation climb, the Q_{def} values can to some extent be comparable to values of Q_{cr} especially in high SFE alloys [27]. For Al, the activation energy in hot torsion has been determined to be 125–180 kJ/mol, while in creep the Q_{cr} has been determined as 155 kJ/mol. However, for austenitic 18/8 stainless steel, which has low SFE, the activation energies were 414 and 314 kJ/mol, for hot torsion and creep, respectively [27]. The difference was attributed to the

occurrence of dynamic recrystallization during hot torsion in austenitic stainless steel [27].

Alloying affects many material properties such as the lattice parameter, stacking fault energy or melting point, and therefore it also affects the Q_{def}. Solute atoms also cause friction stress for gliding dislocations and, therefore, affect the glide controlled creep. In the case of climb-controlled creep, alloying atoms cause solute drag to dislocations [26]. Large concentrations of an alloying element can also markedly alter the SFE and, therefore, the ability of dislocations to cross-slip also affecting the recovery kinetics [27].

However, as pointed out by Briotett *et al.* [33], the calculated Q_{def} value using an empirical hyperbolic sine equation (Eq. 8) is merely an apparent activation energy and does not necessarily relate to any single physical mechanism.

2.2 Flow behaviour of ferrite in hot deformation

The hot deformation flow curves of ferritic stainless steels are typical for materials whose deformation is controlled by dynamic recovery (DRV) [34], i.e. the flow stress increases up to a saturation level, which is achieved at a certain strain and does not generally decrease after that. Therefore, no well-defined peak-stress exists. The steady state stress and the strain at which it is achieved increase with an increasing Zener-Hollomon parameter (Z) [35], i.e. as the temperature decreases and/or the strain rate increases.

Being able to predict the flow behavior during hot deformation is very important when designing the rolling pass schedules. The methods of predicting the flow curves can be divided into three categories: phenomenological models e.g. [31], physically based models e.g. [36–39] and neural network models e.g. [40–42]. Each method has its advantages and disadvantages.

The phenomenological models, e.g. the hyperbolic sine equation (Eq. 8), are based on the Arrhenius equation [31] and consist of fitting a mathematical equation to the experimentally achieved data and are therefore not based on any underlying physical phenomena. The physical models, e.g. Bergström's model [36–38, 43] or the model by Roters et. al [39], are based on the variations of the dislocation density as a result of work hardening and dynamic recovery, i.e. physical phenomena causing variations in the flow resistance. The neural network models involve building up and training the neural network, which is capable of predicting the flow resistance [40].

The empirical models are often rather simple, whereas the physical models may contain multiple inner state variables, which can make the models rather complicated to use. However, the physical models can provide a very accurate flow stress prediction. The neural network models usually require computer programming, and the model development can take a long time. In the current investigation, constitutive equations, i.e. the hyperbolic sine equation (Eq. 8) and Bergström's physical model, were chosen for flow stress modeling. The empirical approach was described in detail in the previous section, whereas Bergström's model will be described in the next section.

2.2.1 Bergström's model

In Bergström's model, which is a physical flow stress model, the flow stress is taken as a combination of work hardening, i.e. increase in the dislocation storage, and DRV, i.e. annihilation of dislocations. The dependence of dislocation density ρ on strain ε is given by the equation [36, 38, 43]:

$$\frac{d\rho}{d\varepsilon} = U - \Omega\rho, \tag{9}$$

where U represents the work hardening rate and $\Omega\rho$ the contribution of DRV through dislocation annihilation and rearrangement. Therefore, Ω is referred to as the coefficient of DRV. U and Ω are considered to be independent of strain. The variations in the dislocation density ρ during the hot deformation can be described as:

$$\rho = \rho_0 \exp\left(-\Omega\varepsilon\right) + \frac{U}{\Omega}\left[1 - \exp\left(-\Omega\varepsilon\right)\right]. \tag{10}$$

The contribution of the dislocation density ρ to the flow stress σ can be expressed using the following relationship [36, 38, 43]:

$$\sigma = \gamma G b \sqrt{\rho}, \tag{11}$$

where γ is the Taylor constant, b is the distance between atoms in the slip direction, i.e. the Burger's vector, and G is the shear modulus. By combining equations 10 and 11, σ can be written as:

$$\sigma = \gamma G b \left[\rho_0 \exp\left(-\Omega\varepsilon\right) + \frac{U}{\Omega}\left(1 - \exp\left(-\Omega\varepsilon\right)\right) \right]^{1/2}. \tag{12}$$

During steady state flow, the dislocation density can be obtained as [36, 38, 43]:

$$\rho_{ss} = \frac{U}{\Omega}. \tag{13}$$

Therefore, the Eq. 11 during steady state flow can be written as:

$$\sigma_{ss} = \gamma G b \sqrt{\frac{U}{\Omega}}. \tag{14}$$

Consequently, in the region where DRV is the controlling process, the flow stress can be expressed using Eq. 14 as:

$$\sigma = \left[\sigma_{ss}^2 - \left(\sigma_{ss}^2 - \sigma_0^2\right)\exp\left(-\Omega\varepsilon\right)\right]^{1/2}, \tag{15}$$

where σ_0 is the initial stress at zero strain at which the dislocation density can be expressed by ρ_0. σ_0 also includes the effect of the initial friction stress, and therefore the value of σ_0 is not equal to zero at zero strain.

The following equation has been proposed for the recovery coefficient Ω at elevated temperatures for situations where the controlling mechanism for recovery is dislocation climb due to vacancies [38]:

$$\Omega = C\left(\dot{\varepsilon}\right)^{-1/3}\exp\left(\frac{-Q_m}{3RT}\right), \tag{16}$$

where C is a material constant and Q_m represents the activation energy for vacancy diffusion.

2.3 Dynamic restoration mechanisms

The restoration processes, recovery and recrystallization, are competing processes which both lead to the softening of the steel [44]. When occurring during deformation, they are called *dynamic recovery* (*DRV*) and *dynamic recrystallization* (*DRX*). The static annealing processes, *static recovery* (*SRV*) and *static recrystallization* (*SRX*), occur after the deformation process during the inter-pass times or hot band annealing [44]. Three different DRX mechanisms have been identified which lead to formation of high angle grain boundaries during deformation at high temperatures: discontinuous dynamic recrystallization (DDRX), geometric dynamic recrystallization (GDRX) and continuous dynamic recrystallization (CDRX).

The dynamic restoration mechanism occurring in high SFE metals is determined by the purity of the metal and by the deformation conditions, i.e. Z [11]. According to the classic work of Glover and Sellars on α-iron [11], the dynamic restoration mechanisms change from DRV under high values of Z, i.e. at low temperatures and high strain rates, to DRX under low Z, i.e. at high temperature and slow strain rate. The dependency of the restoration mechanisms on Z has been later confirmed in multiple studies, e.g. on α-iron [45], on a 26% Cr ferritic stainless steel [16], and on a low C steel in the ferrite region [46].

2.3.1 Discontinuous dynamic recrystallization (DDRX)

DDRX, which is considered to be the conventional form of DRX, occurs through nucleation and growth of new grains in a similar way to SRX [44]. Increasing the purity of the material increases the incidence of DDRX since the number of particles which could pin the grain boundaries decreases [47]. DDRX is often seen as a peak stress in the flow stress curves [29, 48, 49]. However, when DDRX occurs under low Z, i.e. at low strain rate and high temperature, the flow stress exhibits multiple oscillations caused by many cycles of DDRX [47, 48].

In metals with high SFE, such as in ferritic stainless steels or aluminum alloys, the dislocations are unit dislocations, which can cross-slip readily leading to a very intense DRV. DRV not only reduces the stored energy and the driving force for DRX, but also for SRX. Therefore, DDRX is considered unlikely in ferritic stainless steels and other metals with high SFE. However, the nucleation of DDRX has been shown to occur in pure Al [50, 51, 52] or in highly purified α-iron in the ferritic region [11, 45]. Similarly, DDRX has been detected in IF steel during deformation in the ferrite region [53], although it was claimed later that the results were misinterpreted [54]. However, DDRX has not unambiguously been confirmed to occur in ferritic stainless steel.

2.3.2 Geometric dynamic recrystallization (GDRX)

The second mechanism, GDRX, occurs at high strains when the original grains are thinned to about twice the size of the subgrains and are split up geometrically, i.e. new recrystallized grains are formed by *pinching-off* of original grain boundaries [55]. GDRX has been observed in materials which undergo DRV and form subgrains during hot deformation, e.g. in Al and Al-Mg alloys [56–58]. The

grains formed through GDRX are about 2–3 times the subgrain size, whereas SRX usually forms grains of 20–30 times the subgrain size [57].

2.3.3 Continuous dynamic recrystallization (CDRX)

The third mechanism for DRX, CDRX, has no nucleation phase, and the new grains form by the gradual increase of the misorientation of low-angle grain boundaries (LAGBs) [59]. CDRX is a combination of work hardening, DRV and HAGB migration, which is why some authors claim that the mechanism should be referred to as a form of recovery instead of recrystallization [54, 60]. However, since CDRX has become a commonly accepted theory, and the term has achieved a standard role in the metallurgical terminology, it is used in the current study.

Gourdet and Montheillet [59] have proposed the following stages for CDRX:

- Accumulation of dislocations
- Formation of LAGB
- Increase of their misorientation and possible transformation into HAGBs
- Annihilation of internal dislocations and boundaries by moving HAGBs.

During CDRX, many of the recrystallizing grains are still "*in progress*", and therefore a typical feature of the recrystallizing grains is that they are only partially surrounded by a HAGB [61]. When CDRX occurs, the flow curves often exhibit a single smooth maximum, after which a softening state continues up to very high strains (over 30 achieved in torsion) [59]. The subgrain size and the misorientation distribution stabilize after a transient period [61].

CDRX has been identified in high SFE metals such as Al and Al alloys [61–63], ferritic stainless steels [16, 64, 65], in the ferrite region of an IF steel [66], plain low C steels [46, 67, 68] and a microalloyed steel [69].

During the early stages of deformation in the warm deformation range, CDRX can lead to considerable refinement in the grain and subgrain size, and due to the considerable grain refinement potential, CDRX is technologically an interesting phenomenon [59]. When occurring during large strain warm deformation of plain carbon steels [67, 70], ultra-low C steel [71], ferritic stainless steel [72, 73], or a microalloyed steel [69] CDRX can lead to substantial grain refinement and to formation of ultra-fine grained (UFG) materials.

2.4 Static recrystallization

The isothermally recrystallized fraction, X_{rex}, can be expressed as a function of time, t, by an Avrami-type equation [74]:

$$X_{rex} = 1 - \exp\left[-0.693\left(\frac{t}{t_{0.5}}\right)^{n}\right], \tag{17}$$

where $t_{0.5}$ is the time for 50% recrystallization and n is known as the Avrami exponent. The $t_{0.5}$ depends on the deformation conditions, composition and the initial grain size as follows e.g. [75]:

$$t_{0.5} = C_{0.5}\varepsilon^{p}\dot{\varepsilon}^{q}d^{s}\exp\left(\frac{Q_{app}}{RT}\right), \tag{18}$$

where $C_{0.5}$ is a constant depending on the chemical composition, ε is the true strain, $\dot{\varepsilon}$ is the true strain rate, d the grain size, and Q_{app} the apparent activation energy for SRX. The exponents p, q and s are material constants, which describe the powers of strain, strain rate and the grain size respectively [76]. The Avrami exponent n provides information about the nucleation mechanism of SRX and is generally considered to be independent of the temperature [75].

2.5 Effect of grain orientation

As shown by the extensive studies by Tsuji *et al.* on ferritic stainless steel single crystals [77–79], the deformation and recrystallization in ferritic stainless steels are highly dependent on the orientation of the deformed grain. After hot deformation, the size of the subgrains varied, being largest in the [001] crystal and much finer in [111] and [133] crystals [77]. The differences in the amount of dislocation density between different crystals affected the SRX kinetics during subsequent annealing. However, the SRX kinetics was not solely dependent on the overall dislocation density but also on the local misorientation of the deformed structures [77].

Ferritic stainless steels, having a BCC crystal structure, tend to develop strong fiber textures during deformation and recrystallization annealing. The texture of stabilized ferritic stainless steel can most often be described using the α (<110>//RD) and γ (<111>//ND) fibers [17, 80, 81]. The most common locations

of the intensity maxima, together with the locations of the α, γ and ε fibers, are presented in a $\varphi_2 = 45°$ ODF plot in Fig. 2.

Another common feature of the textures of ferritic stainless steels is the strong texture gradients in the thickness direction of the rolled strip or plate [80–82]. In the center of hot rolled plate, a strong α fiber texture is formed due to plane strain deformation conditions and dynamic recovery [7, 8, 80]. The intensity maxima are often observed at {001}<110> at the beginning of the α fiber and along the α fiber at {112}<110> and {111}<110> [81]. A shear texture, which is composed mainly of the Goss texture with {011}<100> orientation, forms at the surface layer as a result of shear deformation. [7, 80].

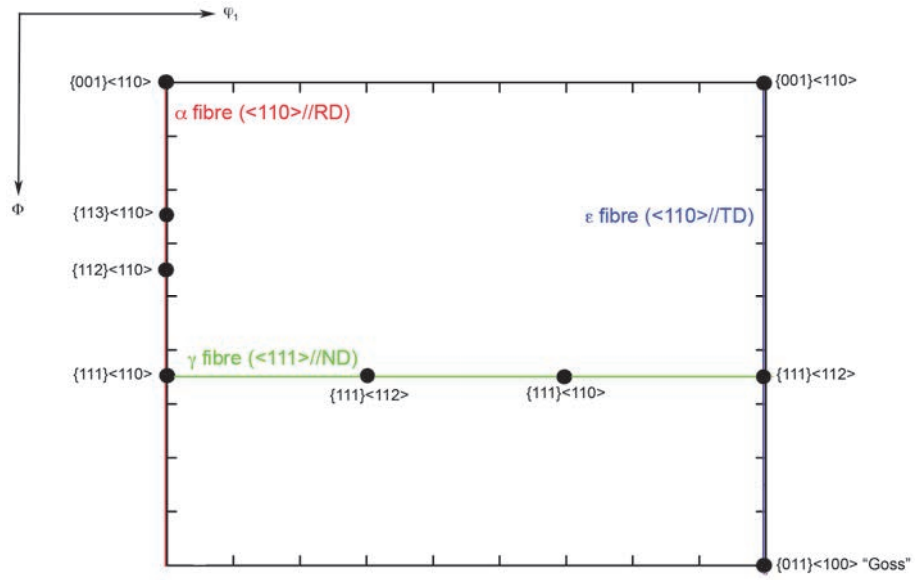

Fig. 2. The $\varphi_2 = 45°$ ODF showing the locations of the most important texture maxima together with the locations of the α, γ and ε fibers.

During cold deformation, the intensity of the α fiber between {001}<110> and {112}<110> increases continuously as the degree of the deformation increases [17, 81]. Simultaneously, the dominant intensity maxima along the γ fiber at {111}<112> increases up to the rolling reductions of ~70% after which no increase occurs due to intense shear band formation in the {111}<112> oriented grains [81]. During post-deformation annealing of ferritic stainless steels, the strong α fiber is removed for the most part between {112}<110> and {111}<110>, and the main texture component is often observed at {111}<112> along the γ fiber.

The intensity maxima at {001}<110> at the beginning of α and ε fibers also remain after SRX [17].

The texture development during annealing after both hot and cold deformation can be caused either by oriented nucleation or by oriented growth, or as a combination of both [8, 81]. The oriented nucleation theory is based on the idea that nuclei of specific orientations form faster than nuclei of other orientations depending on the orientation of the deformed grain e.g. [83]. For the texture development of ferritic stainless steels, oriented nucleation is typical of γ fiber grains and they are the first to nucleate [83]. As a result of oriented nucleation, the {111}<112> orientation may often develop into {111}<110> grains, and vice versa [8].

The oriented growth theory is based on the idea that some boundaries have higher mobility than others due to specific orientation relationships [83]. Therefore, oriented growth of recrystallizing grains occurs when there is a favorable orientation relationship between the deformed and recrystallizing grain, e.g. 35° around <110> transverse direction, namely a Σ9 coincident site lattice (CSL) boundary, which is very close to the ideal relationship of 27° <110>, which is known for its high mobility [81]. The recrystallization of the α fiber grains occurs generally through oriented growth [81]. For instance, the Σ9 CSL boundary, can be found between {011}<110> grains and {111}<112> deformation texture component [81], and therefore {011}<110> grains can grow, consuming the {111}<112> oriented deformed grains. However, also γ fiber grains can take advantage of the high mobility of the special boundaries, and the common {111}<112> recrystallization component can grow through selected growth into adjacent {001}<110>–{112}<110> grains [8].

Small stable particles, i.e. precipitates, affect the texture formation during recrystallization, and a new recrystallization texture component {557}<583> may be introduced instead of the classical {111}<112> and minor Goss components [8]. This is due to the particle-drag effect on non-special boundaries. Particle drag hinders the movement of the boundaries, i.e. recrystallization, whereas CLS boundaries are not affected [8]. The mechanism is called *grain boundary selective particle drag* [8].

The grain orientation is also known to affect the SRX kinetics due to the orientation dependency of the Taylor factor, which is a measure of the total amount of slip occurring per unit of imposed strain [20, 83]. Therefore, also in the deformed state, the amount of substructure and the amount of stored energy varies as a function of grain orientation [83]. The γ fiber grains have a high Taylor factor,

and therefore a high dislocation density, whereas the α fiber grains have a low Taylor factor [83]. Therefore, the γ grains are the first to recrystallize [83].

2.6 Flow localization and the formation of in-grain shear bands

During deformation in the warm deformation temperature range, flow localization may occur in the γ fiber grains and lead to the creation of deformation bands, which are limited to the area of one single grain, and can therefore be termed *in-grain shear bands* [21, 84, 85]. In-grain shear bands do not form during deformation at high hot deformation temperatures due to intensive DRV, which prevents flow localization. The in-grain shear bands are mostly inclined at angles of 30–35° to the rolling direction [21], however, the angle has also been reported to be much broader, i.e. ±20–60° [86]. The in-grain shear bands differ from the conventional shear bands in that they do not cross grain boundaries [86].

The occurrence of in-grain shear bands is affected by dynamic strain ageing (DSA) [21, 23, 25], and therefore it is temperature dependent in steels, which contain solute C, such as, in low C steels [21]. However, such temperature dependency is not observed in IF-steels where moderate in-grain shear bands form, regardless of the deformation temperature during deformation in the ferrite region [21, 23–25].

The formation of in-grain shear bands causes grains to split up and weakens the deformation textures [21], and it has also been proposed [21] that they transfer the flow away from the matrix, which in turn retards grain rotations so that the number of grains reaching stable end orientations decreases. On the other hand, sharpened deformation textures are formed in the absence of in-grain shear bands [21, 25].

The in-grain shear bands act as preferential nucleation sites for SRX due to the fact that they are associated with large orientation gradients that accelerate SRX kinetics [20, 22]. The nucleation of SRX in an in-grain shear band in an {111}<112> oriented grain will cause lattice rotations to either Goss or <111>//ND orientations depending on the “severity” of the in-grain shear band; the rotations to Goss took place mainly in the severe in-grain shear bands, which formed only in the low C steels [20, 22, 23]. The formation of the Goss recrystallization texture occurs more readily in the in-grain shear bands with high 35° orientation than in the lower, 20° oriented, shear bands, i.e. in the materials and conditions where the driving force for flow localization is higher [20].

The in-grain shear bands present in IF steels are described as “moderate” regardless of the deformation temperature, and therefore, Goss rarely nucleates in the IF steels [23]. Most of the grains, which have nucleated in the in-grain shear bands in IF steels, have γ fiber orientations, i.e. <111>//ND.

2.7 Lowering the hot deformation temperature

Various methods have been tried for improving the texture structure of ferritic stainless steels hot bands. These include cross-rolling, i.e. changing the rolling direction between the deformation passes [87], and increasing the strain rate during rolling in the ferrite region [88]. According to the literature, the most promising method seems to be lowering the hot deformation finishing temperature of multi-pass hot deformation to ~750 °C, which should lead to the formation of in-grain shear bands and nucleation of γ fiber grains in them as shown earlier for 17% Cr and 21% Cr ferritic stainless steels [13–15, 89].

The favorable effect of lowering the hot deformation finishing temperature has been attributed to the reduced effectiveness of DRV leading to higher stored energy, and to the formation of in-grain shear bands, which not only act as nucleation sites for SRX grains and promote the SRX kinetics, but also enhance favorable texture formation by increasing the number of recrystallized grains oriented with <111>//ND [15].

During deformation of ferritic stainless steel at decreased temperatures, grain rotations are increased and texture development towards stable components is promoted; even the {001}<110> orientation at the beginning of the α fiber has been observed to rotate towards relatively stable {112}<110> orientation and γ fiber [13, 14]. During subsequent hot band annealing, the α fiber has been observed to almost completely disappear whereas the γ fiber is intensified [15]. After warm rolling and subsequent annealing, the γ fiber has been shown to be more uniform than in conventionally hot rolled material, leading to enhanced deep drawability in ferritic stainless steels [14, 15]. However, the improved deep drawability has also been attributed to differences in precipitation behavior at the conventional high hot rolling temperature and warm rolling temperatures, which affect the texture formation during later processing stages [90].

3 Experimental

3.1 Materials

Six different stabilized ferritic stainless steels were used as test materials. The compositions of the steels are such that austenite–ferrite phase transformation does not occur, i.e. the steels are fully ferritic in the hot deformation temperature range. Materials #1–#5 were laboratory cast ingots of 35 kg, which were hot rolled in a laboratory hot rolling mill at 1100 °C from 48 mm down to the thickness of 15 mm with 3 passes. Material #6 was delivered as 35 mm thick transfer bar. The chemical composition (in weight percent) of the steels is listed in Table 1. The main focus of the studies has been on the materials #3 and #6, which both contain 21% of Cr.

Table 1. The chemical composition (in wt.%) and the initial grain size (μm) of the steels investigated.

Steel	Cr	C	N	Ti	Nb	Ni	Si	Cu	Mn	Initial grain size
#1	12	0.007	0.008	0.35	0.12	0.2	0.24	0.4	0.35	173
#2	18	0.007	0.009	0.33	0.11	0.2	0.25	0.4	0.31	134
#3	21	0.004	0.008	0.33	0.11	0.2	0.30	0.4	0.32	157
#4	24	0.005	0.009	0.34	0.11	0.2	0.29	0.4	0.31	229
#5	27	0.006	0.01	0.30	0.11	0.2	0.31	0.4	0.33	123
#6	21	0.02	0.02	0.15	0.25	0.2	0.6	0.3	0.35	75

Prior to the compression tests, a solution annealing at 1100 °C for 2 minutes was carried out as a part of each test regimen before the actual compression. The purpose of the solution annealing was to dissolve any carbides present in the microstructure, so that they would not interfere with the dynamic and static restoration processes. However, the success of this procedure was not verified. The “initial” grain sizes were measured from the specimens, which were solution annealed and quenched immediately after the annealing, i.e. prior to the deformation. The initial grain sizes measured are also presented in Table 1.

3.2 Hot compression tests

Compression tests at elevated temperatures were used for simulating hot deformation and the hot rolling of the steels. By employing physical simulations

of hot deformation, it was possible to accurately alter the main processing parameters of the hot deformation, namely the deformation temperature, strain and strain rate. Two test machines were employed: a Gleeble 1500 Thermomechanical simulator, located at the Materials Engineering Laboratory at the University of Oulu, and a Thermomechanical Compression Machine (TMC), located at the Department of Materials Science and Engineering at The University of Sheffield, UK.

Table 2 presents the test materials, compression test machines and the specimen shapes, and the equipment for microstructure characterization employed for Papers I–V.

Table 2. The test materials, compression test methods and microstructure characterization methods employed in each paper.

Paper	Steel	Compression test method	Microstructure characterization method
I	#1–#5	Gleeble axisymmetric	-
II	#3	Gleeble axisymmetric	Zeiss Ultra Plus FEG-SEM + HKL EBSD detector
III	#6	TMC plane strain	Zeiss Sigma FEG-SEM + EDAX EBSD detector, Hitachi H7600 TEM
IV	#6	TMC plane strain	Zeiss Ultra Plus FEG-SEM + HKL EBSD detector, Hitachi H7600 TEM
V	#6	Gleeble plane strain	Zeiss Ultra Plus FEG-SEM + HKL EBSD detector

3.2.1 Gleeble axisymmetric and plane strain compression tests

Gleeble compression tests were performed either on axisymmetric or plane strain specimens using a single-hit test regimen. Axisymmetric compression tests were used in Papers I and II, whereas plane strain compression tests were carried out for Paper V. The axisymmetric specimens were cylindrical 10 mm in diameter and 12 mm high specimens, and they were cut with their axes parallel to the normal of the rolling plane. The plane strain specimens were 15 mm in length, 10 mm in width and 6 mm in thickness. The width of the compression anvil was 5 mm. The plane strain specimens were cut so that the rolling, transverse and normal directions of the transfer bar were maintained during the plane strain compression tests.

In axisymmetric Gleeble compression tests the specimens were reheated at the rate of 20 °C/s to 1100 °C and held for solution annealing for 120 s prior to the deformation. Thereafter, the specimens were cooled at the rate of 10 °C/s to the deformation temperature (950, 1000 or 1050 °C). The specimens were

compressed in a single hit to the true strain of 0.2–0.6 at a constant strain rate between 0.01 and 1 s^{-1}. After the compression, the specimens were either water-quenched to room temperature immediately after the deformation or annealed at the deformation temperature for 10–180 s, after which they were air-cooled to room temperature.

Solution annealing was similarly applied to the plane strain specimens using the same heating and cooling rates as for the axisymmetric specimens. The deformation temperatures used in plane strain compression tests were 550, 600, 750, 800 and 950 °C, and the applied true strain was 0.5 using strain rate of 1 s^{-1}. The specimens were water-quenched to room temperature immediately after deformation. However, some specimens were reheated right after the quench to 750 or 950 °C for recrystallization annealing.

3.2.2 TMC plane strain compression tests

Only plane strain compression tests were performed on the TMC (pictured in Fig. 3). TMC plane strain specimens were larger than the Gleeble plane strain specimens, and were sized 60 × 30 × 10 mm, while the width of the compression anvil was 15 mm. A schematic picture of a deformed TMC plane strain specimen with the dimensions is showed in Fig. 4. As with the Gleeble plane strain specimens, the directions of the rolling, transverse and normal directions of the transfer bar were maintained during the TMC compression tests.

Two different test regimens were used in TMC plane strain compression tests: a single-hit test regimen to investigate the dynamic microstructure and texture evolution as a function of strain (Paper III), and a triple-hit regimen to simulate multi-pass hot rolling (Paper IV). In both test regimens, the specimens were reheated at the rate of 10 °C/s to 1100 °C for solution treatment, held for 120 s and cooled at 10 °C/s to the deformation temperature which was either 1050 °C or 950 °C. In the single-hit test regimen (Paper III), two different deformation temperatures and strain rates were used (950 or 1050 °C and 0.1 s^{-1} or 10 $^{-1}$, respectively). The applied true strains were 0.2, 0.5, 1 and 1.5.

Fig. 3. The TMC machine.

In the multi-compression test regimen, the specimens were deformed to strains of 0.4 or 0.5 in each pass using a strain rate of 20 s^{-1}. The inter-pass time was 20 s. The first two passes were performed at 950 °C; however, the temperature of the third pass was either 950, 800 or 650 °C. The cooling between the second and third pass, if necessary, was performed within the 20 s of inter-pass time. After the third and final pass, the specimens were either water-quenched to room temperature or to 650 °C from where the specimens were cooled slowly over 20 minutes to 250 °C at a constant cooling rate of approximately 20 °C/min. The process parameters used in the physical simulations were comparable to the deformation conditions in the industrial Steckel mill rolling.

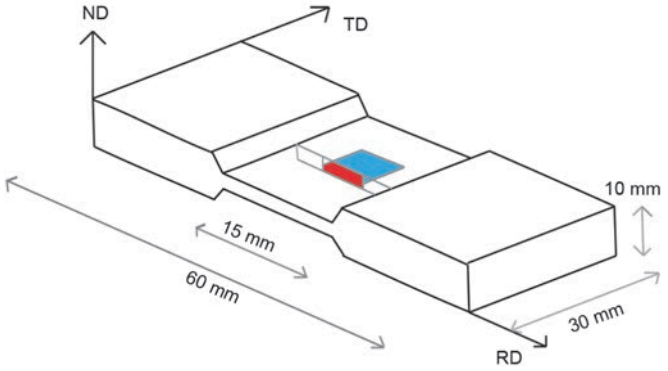

Fig. 4. An illustration of the TMC specimen, which shows the dimensions of the specimen, the compression anvil and the locations of the sections cut for EBSD (in red) and TEM (in blue) studies. [Paper III, published by permission of Elsevier Ltd.]

3.3 SEM-EBSD

The microstructures and textures were investigated using electron backscatter diffraction (EBSD) on a Zeiss Ultra Plus FEG-SEM with an HKL EBSD detector or on a Zeiss Sigma FEG-SEM with an EDAX EBSD detector. The accelerating voltage was 15 kV or 20 kV and step size either 1, 0.5 or 0.2 μm depending on the magnification (300×, 500× or 1000×). The magnification was chosen based on the grain size, the degree of deformation of the material being investigated, and also depending on whether the purpose was to measure macrotexture (low magnification) or to study detailed microstructural features (higher magnifications). The low magnification EBSD maps were also used for determining the statically recrystallized fractions (Paper II and V).

For EBSD studies, the specimen surfaces were polished using a diamond suspension down to 1 μm, after which a chemical polishing was applied using a 0.05 μm colloidal silica suspension. The sections used for the SEM-EBSD studies were cut from the middle of the compressed specimens where the degree of deformation was closest to the intended strain. In the case of TMC plane strain specimens, the locations of the sections cut for EBSD studies are shown in red in Fig. 4.

3.4 TEM

The structural features were examined in a transmission electron microscope Hitachi H7600 operated at 120 kV. Thin foils were prepared by twin jet electropolishing of 3 mm disks, punched from the specimens, using a solution of 10% perchloric acid in acetic acid electrolyte. The sections of the TMC plane strain specimens used for TEM thin foil specimens are shown in blue in Fig. 4. The TEM investigations were performed at the University of Louisiana at Lafayette, USA, by Professor Misra's team.

4 Results

4.1 Flow resistance

The flow resistance of the steels #1–#5 was investigated in Paper I and on the steel #3 in Paper II. Typical flow curves for ferritic stainless steel in the hot working temperature range are presented in Figs. 5 and 6.

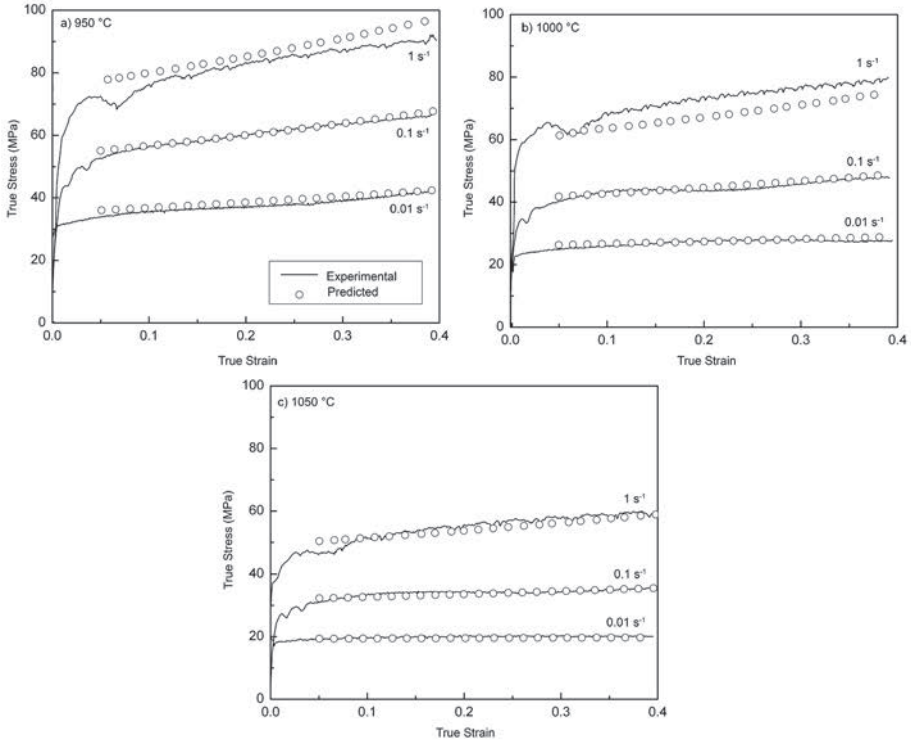

Fig. 5. Comparison between the measured and calculated flow stress at a) 950 °C, b) 1000 °C and c) 1050 °C for steel #3 [Paper II, published by permission of Elsevier Ltd.].

It can be seen that there was only a short intense work hardening stage at the beginning of the deformation, after which a slight work hardening continued up to high strains, or a steady state was achieved, depending on Z. A true steady state flow is achieved only at high temperatures and low strain rates, i.e. under low Z. Limited work hardening indicated that DRV was very effective during the

deformation. Furthermore, the flow curves did not exhibit a single-peak behavior or undulations. The average flow stress, which was determined over the strain range of 0–0.4, was dependent on the deformation conditions, i.e. Z, as seen in Fig. 7.

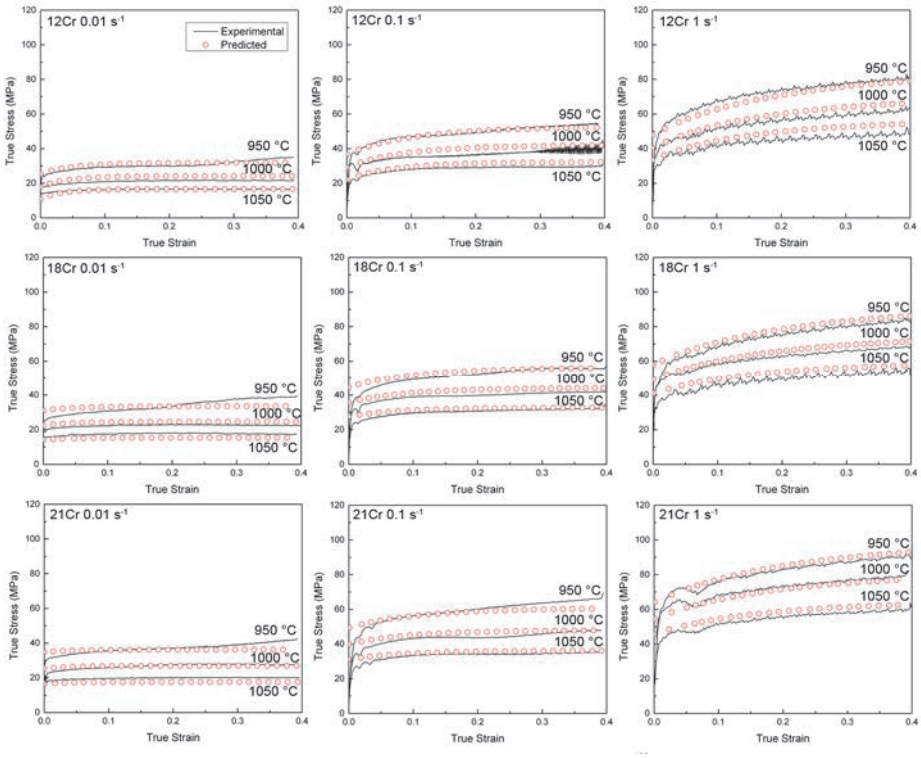

Fig. 6. The experimental and calculated flow stress curves for 12–21% Cr steels (#1–#3) during deformation at 950–1050 °C at 0.01–1 s^{-1} [Paper I, published by permission of Elsevier Ltd.].

The Cr content increased the flow stress through solid solution strengthening as shown in Paper I. As seen in Fig. 6, The Cr content did not affect the shape of the flow curves, which were determined solely by the deformation conditions, i.e. Z. The effect of Z on the flow stress measured after straining to true strains of 0.2 and 0.4 on test materials with 12–27% Cr is presented in Fig. 8. Furthermore, the greater grain size of the 24% Cr containing material (steel #4) did not seem to affect the flow stress values as much as the Cr content did.

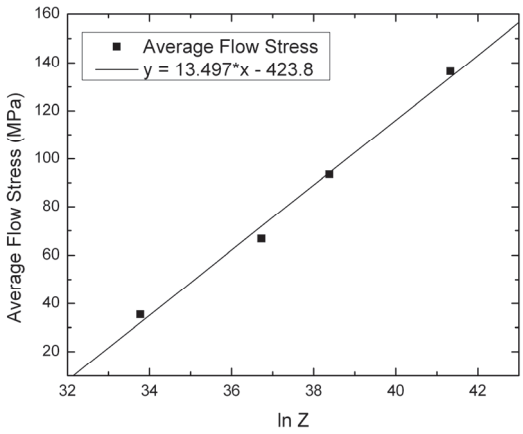

Fig. 7. Average flow stress in TMC plane strain deformation measured for the material #6 as a function of the Zener-Hollomon parameter. The average flow stress was calculated for strain range 0–0.4. [Paper III, published by permission of Elsevier Ltd.]

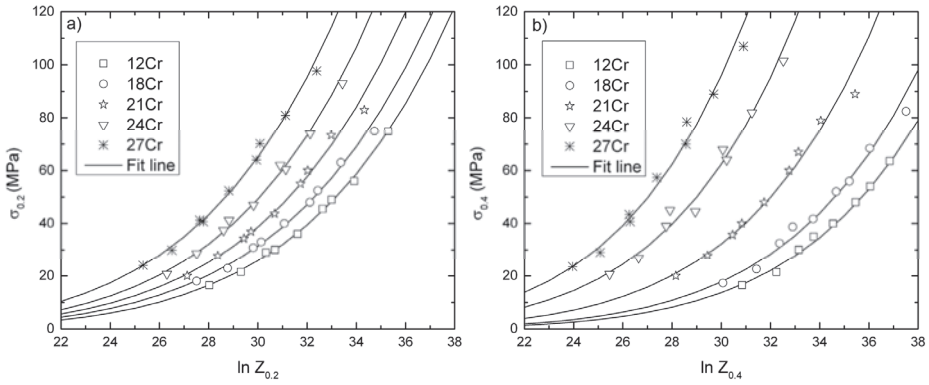

Fig. 8. The effect of Z on the measured flow stress at a) 0.2 and b) 0.4 strains. The fit line represent the power equations fitted for the experimental data. [Paper I, published by permission of Elsevier Ltd.]

4.1.1 Activation energy for deformation

The apparent activation energy for deformation, Q_{def}, was determined as a part of flow stress modeling for the 12–27% Cr containing steels (Steels #1–#5) in Paper I. As seen in Fig. 9, an increase in the Cr content reduced Q_{def}, and the values of

Q_{def} varied from 359 kJ/mol to 329 kJ/mol while the Cr content varied in the range 12–27%. The error bars in Fig. 9 represent the standard error, and it can be seen that they overlap, which means that the difference is not statistically significant.

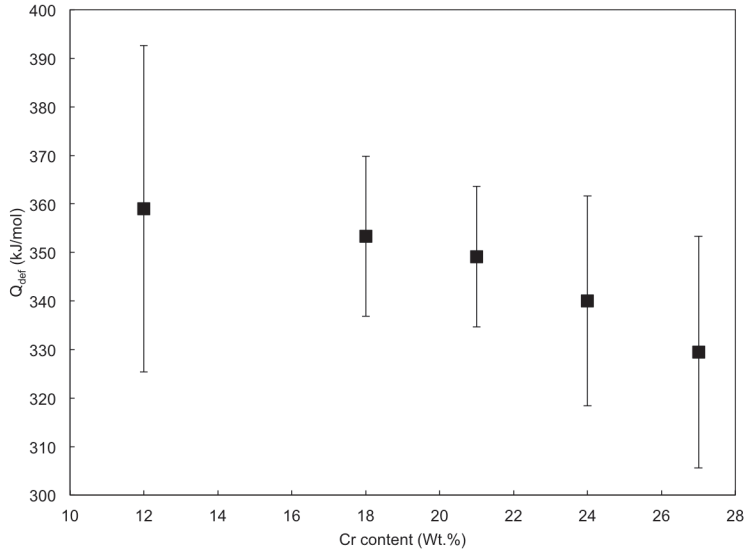

Fig. 9. The effect of Cr content on Q_{def}. The error bars represent the standard error [Paper I, published by permission of Elsevier Ltd.].

4.1.2 Constitutive equations

In Paper II, the hyperbolic sine equation (Eq. 8) was applied for calculating the flow stress curves for steel #3, which contains 21% Cr. The temperature and the strain rate range used was 950 °C to 1050 °C, and 0.01 s^{-1} to 1 s^{-1}, respectively.

σ in Eq. 8, can be taken as the peak stress, σ_p, e.g. [30] or the steady state stress, σ_{ss}, e.g. [73]. However, in the case of deformation of ferritic stainless steels, a peak stress does not appear nor is a steady state stress achieved under every Z. Therefore, in order to apply the hyperbolic sine equation for the flow stress prediction, the variation of the flow stress as a function of strain had to be incorporated into the constitutive equation. An approach developed by Slooff *et al.* [91] was chosen for this purpose, in which the effect of strain is incorporated into the parameters of the constitutive equation. The parameters were defined for

different strain intervals, and a linear or a polynomial fit was applied to describe the effect of strain. The method has also been applied successfully by a number of other authors, e.g. [92–94].

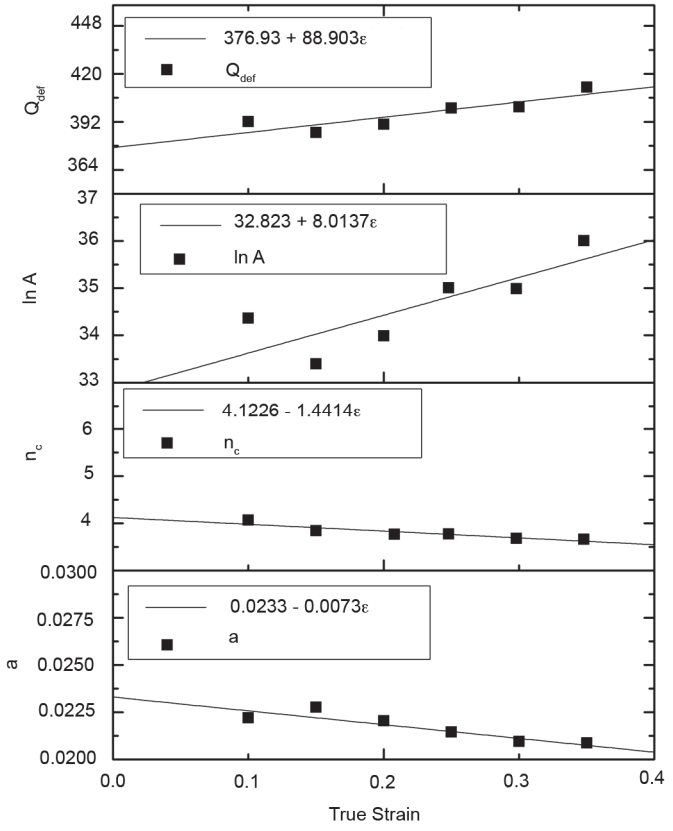

Fig. 10. Variation of Q_{def}, ln$A$, n_c and a as a function of strain [Paper II, published by permission of Elsevier Ltd.].

The variation of Q_{def}, ln$A$, n_c, and a as a function of strain with the linear fits and their equations in Fig. 10.

The experimentally achieved and the calculated flow curves using the hyperbolic sine equation (Eq. 8) are presented in Fig. 5. It can be seen that the fit is quite good, and the greatest difference between the experimental and calculated flow stress values appeared during deformation at 1 s^{-1} at 950 °C and 1000 °C, i.e. under the highest Z.

4.1.3 Bergström's model

In Paper I, a dislocation-based flow stress model, i.e. Bergström's model, which incorporates the solid solution strengthening caused by the various Cr contents, was used for predicting the flow stress for materials #1–#5, which contain 12 to 27% Cr. It was noticed that an increase in the Cr content increased the flow stress but did not affect the shape of the flow curves, as seen in Fig. 6 where the flow curves for steels #1–#3 are presented.

In order to calculate the flow curves using Eqs. 14 and 15, the values for γ and b were taken as 0.88 and 2.5×10^{-10} m, respectively [36, 38]. Ω, which was found to be independent of the Cr content, was calculated using Eq. 16. As a rule of thumb, Q_m in Eq. 16 can be taken as $0.5Q_{diff}$ where Q_{diff} represents the activation energy for self-diffusion [38]. The value for Q_{diff} was taken as 239 kJ/mol [95]. It was discovered that a common value of 200 for the constant C was suitable for every deformation condition and test material. However, no exact values were to be found for G for high-Cr ferritic stainless steels at high temperatures. Therefore, the values for G at 21–630 °C given by Bergström [38] were employed for calculating the G at 950–1050 °C using linear extrapolation. Since the value of G for ferritic iron was determined as 78500–60800 MNm^{-2} for the temperature range of 21–630 °C [38], values for G at the current temperatures 950, 1000 and 1050 °C were calculated to be 52,000, 51,000 and 50,000 MNm^{-2}, respectively. These calculated values may not be correct. However, they are not crucial for the employment of the model, and therefore they were considered to be sufficient.

The two remaining parameters, which had to be calculated in order to employ Eqs. 14 and 15 in flow curve predictions, were U and σ_0. They were found to be dependent on the Cr content as well as on the deformation conditions, i.e. Z. However, when calculating the values for U and σ_0 it was noticed that the linear fit between U and σ_0 and Z was not very good, and therefore two modified Zener-Hollomon parameters, Z' and Z'', were developed as in [96, 97]:

$$Z' = \dot{\varepsilon}^{0.5} \exp \frac{Q_{def}}{RT}, \tag{19}$$

$$Z'' = \dot{\varepsilon}^{0.9} \exp \frac{Q_{def}}{RT}. \tag{20}$$

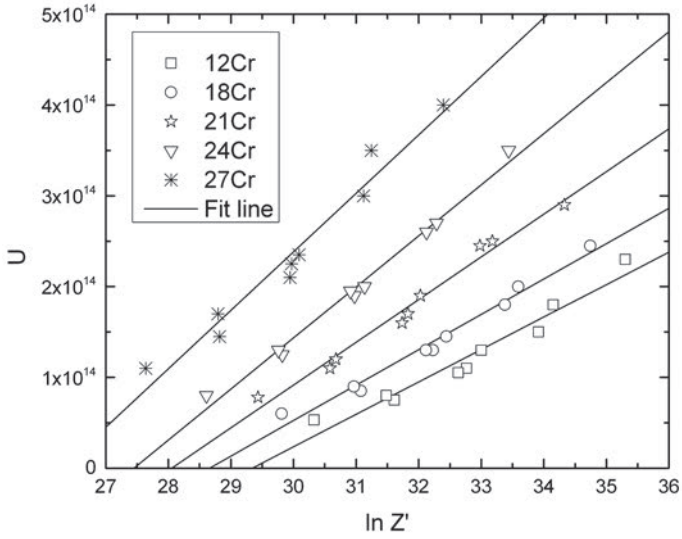

Fig. 11. U as a function of Z' for 12–27% Cr steels [Paper I, published by permission of Elsevier Ltd.].

The experimental values of U as a function of $\ln Z'$ for all test materials is presented in Fig. 11 together with the linear fits. The equations for the linear fits ($U = a \times \ln Z' + b$) for each composition were used to model a and b as a function of the Cr content. It was found that U can be presented as a function of the Cr content and Z' by combining $a = f(\%Cr)$, $b = f(\%Cr)$ and $U = f(\%Cr, Z')$. U was expressed by using the following empirical equation:

$$U = 2.074\times10^{13}\exp\left(0.04084\left(\%Cr\right)\right)\ln Z' - 4.515\times10^{13}\left(\%Cr\right) - 4.326\times10^{14}, \qquad (21)$$

where (%Cr) represents the Cr content in weight-%.

σ_0 was modeled in a similar way to U and it was expressed as a function of Cr content and Z'' by using the following equation, which was determined similarly as the Eq. 21:

$$\sigma_0 = 3.832\exp\left(0.029\left(\%Cr\right)\right)\ln Z'' - 3.801\left(\%Cr\right) - 98.023. \qquad (22)$$

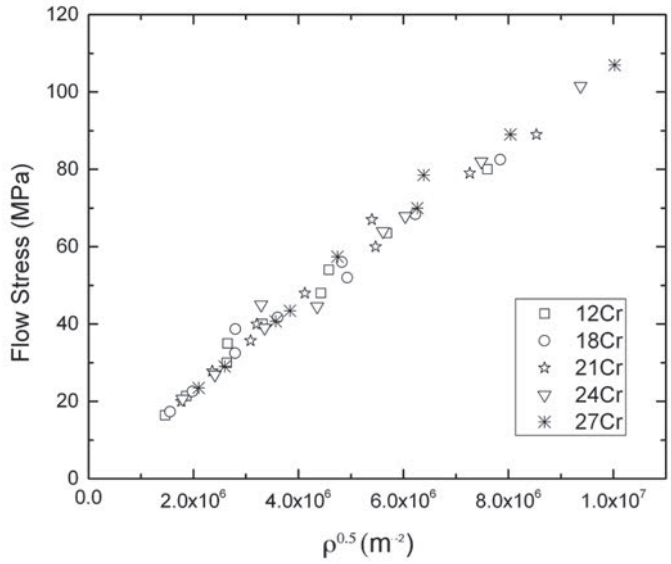

Fig. 12. Estimated dislocation density square roots compared to the measured flow stress at 0.2 strain [Paper I, published by permission of Elsevier Ltd.].

Because the effect of Cr was incorporated into the model by adding two empirical equations, the developed model was only partially physical. Altogether, the model consisted of four equations, out of which two were physical (Eqs. 15 and 16) and two empirical (Eqs. 21 and 22). The calculated flow curves for the #1–#3 steels are presented in Fig. 6. The calculated dislocation densities, ρ, using Eq. 13, varied from 2.13×10^{12} m^{-2} for the steel containing 12% Cr (#1) under the lowest Z (1050 °C, 0.01 s^{-1}) to 1×10^{14} m^{-2}, in the case of the 27% Cr steel (#5) under the highest Z (950 °C, 1 s^{-1}). The corresponding measured flow stress values were 16.5 MPa and 107 MPa, respectively. In Fig. 12 the dislocation densities are presented as a function of the flow stress.

4.2 Dynamic microstructure evolution

The dynamic microstructure evolution of steel #6 under $Z = 1 \times 10^{14}$–1×10^{17} s^{-1} was investigated in Paper III. The following investigation is divided according to the governing deformation conditions, i.e. low, medium and high Z. High Z deformation conditions were also employed in Paper IV and the results are included in the following chapter which focuses on the microstructure evolution

under high Z. The black boundaries in the EBSD maps represent the HAGBs with misorientation greater than 15°, while the yellow and white boundaries represent the LAGBs with misorientations of 5°–15° and 2°–5°, respectively.

4.2.1 Low Z ($Z \approx 1 \times 10^{14}\ s^{-1}$, $\sigma \leq 40$ MPa)

The dynamic microstructure evolution under 1050 °C and 0.1 s^{-1}, i.e. the lowest Z, is presented in Fig. 13 together with the corresponding flow stress curves. It can be seen in Fig. 13 that dislocation annihilation, i.e. DRV, was very effective under low Z, and therefore very few LAGBs had formed. The subgrain structure was rather coarse, and some subgrains were abnormally large as seen in Fig. 13c) and 13d). Quite often the subgrains were only partly surrounded by an HAGB. Due to the low Z, the LAGBs were able to migrate, and as a result of coalescence of LAGBs occurred and new segments of HAGB were formed.

After straining to the highest strain used in the preset investigation, 1.5, some of the new recrystallized grains, which were completely surrounded by a HAGB, were observed to contain substructure, i.e. they were deformed. This indicates that these grains had formed dynamically. The dynamically formed structure after straining to 1 and 1.5, looks very similar, and therefore it seems that a steady state of microstructure evolution was achieved. DRV was so efficient that the high strain was accommodated without significant changes in the microstructure. It was concluded that the form of DRX was CDRX due to very efficient DRV. Also, the fact that some grains were only partly surrounded by an HAGB supports the conclusion. Furthermore, the deformation under low Z does not lead to great grain refinement; however, a steady state in the intercept length between LAGBs and HAGBs, which gives indications of the subgrain and grain size, respectively, was achieved at the strain of 0.5, as seen in Fig. 14a) and b).

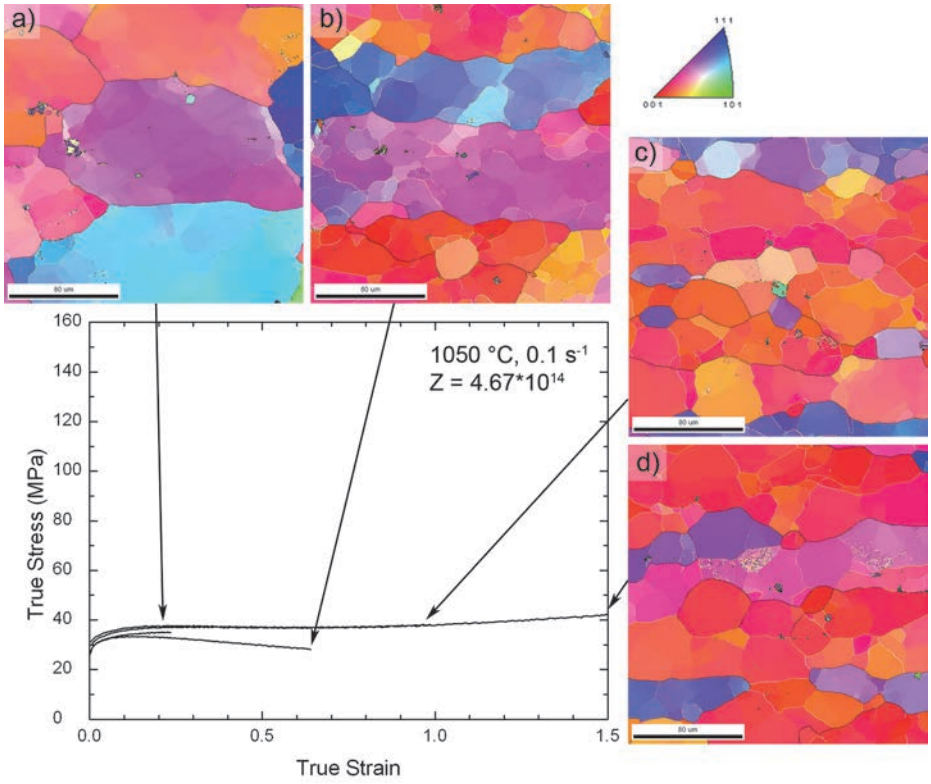

Fig. 13. Flow stress curves and IPF-Z EBSD maps of the dynamically formed microstructures under Z = 4.67 × 10^{14} s^{-1} (1050 °C, 0.1 s^{-1}) after straining to a) 0.2, b) 0.5, c) 1 and d) 1.5. The micron bar is 80 µm long. [Paper III, published by permission of Elsevier Ltd.]

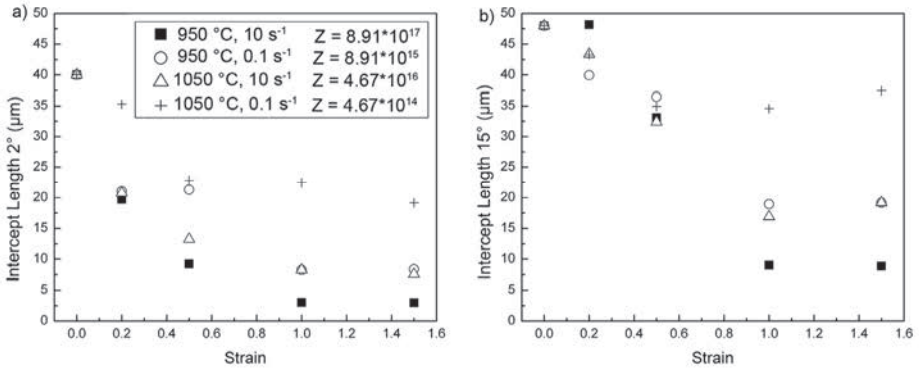

Fig. 14. Intercept length between a) 2° and b) 15° boundaries as a function of strain [Paper III, published by permission of Elsevier Ltd.]

4.2.2 Medium Z ($Z \approx 1 \times 10^{15}$–$1 \times 10^{16}$ s^{-1}, 40 MPa < σ < 120 MPa)

There were many similarities in the microstructures formed under $Z = 1 \times 10^{15}$ and $Z = 1 \times 10^{16}$ s^{-1}. After deformation at 1050 °C at 10 s^{-1}, recrystallized grains had nucleated adjacent to TiN particles as a result of particle-stimulated nucleation (PSN) and at the original grain boundaries. It was concluded that the grains had likely formed statically during the 0.4 s delay period between the deformation pass and quench. After deformation at 950 °C, the number of recrystallized grains was lower than at 1050 °C.

Due to higher Z during deformation at 1050 °C at 10 s^{-1}, the DRV was slightly less effective than during deformation at 950 °C at 0.1 s^{-1}, and therefore more dislocation storage was created during deformation at 1050 °C and 10 s^{-1}. The measured flow stresses were ~80–100 MPa and ~60 MPa, at 1050 °C and 950 °C, respectively. Higher Z at 1050 °C and 10 s^{-1} resulted in a higher number of LAGBs than under $Z = 10^{15}$ s^{-1} (950 °C, 0.1 s^{-1}). Under the lower Z, grain boundary bulging was detected already after straining to 0.2, which can be taken in some cases as an early indication of DDRX. Also, new segments of HAGB had formed after straining to 1.

In both specimens deformed under medium Z, dislocation accumulation was greater than under the lowest Z, which might have allowed DDRX to nucleate. However, due to the high SFE and relatively high impurity level of the steel investigated, the more likely restoration mechanism is DRV and CDRX under both Z. However, the recrystallization mechanism could not be verified due to the delay period between the deformation pass and quench.

4.2.3 High Z ($Z \approx 1 \times 10^{17}$ s^{-1}, $\sigma \geq 120$ MPa)

The highest Z deformation conditions were the least favorable for DRV. Deformation resulted in numerous LAGBs, which were often aligned either at ~35° to the rolling direction or parallel to the RD depending on the orientation of the deformed grain. The distance between LAGBs and HAGBs was also significantly smaller than under low Z deformation, as seen in Fig. 14.

After straining to 1 and especially to 1.5, the original grains became heavily flattened, as seen in Fig. 15. Recrystallized grains were observed at the original grain boundaries, and they were much finer than those formed under low Z, as seen in Fig. 13. The recrystallization mechanism could not be verified, but the initiation of GDRX might have taken place at higher strains of 1 and 1.5, where pinching-off of new grain segments, was observed. On the other hand, the new grains might have nucleated through SRX, especially the ones adjacent to the TiN particles. DDRX was considered unlikely due to high Z. However, CDRX might have taken place, since CDRX has been detected under heavy warm deformation conditions.

The decrease in the flow stress, which was observed with straining to 1.5, was due to decrease in the strain rate during the experiment.

In Paper V, the effect of lowering the deformation temperature from 950 °C to 550 °C was investigated. For the deformation at 750, 600 and 550 °C, the calculated values for Z were 6.6×10^{17}, 7.6×10^{20} and 1.4×10^{22} s^{-1}, respectively. Lowering of the deformation temperature to the high Z region from the conventional hot rolling temperatures had two main effects. Firstly, DRV became increasingly more difficult and, therefore, the dislocation storage was increased in the microstructure, which was evident based on the increased number of LAGBs at the lower deformation temperatures. Secondly, lowering the deformation temperature to 800 °C and below caused flow localization and the formation of in-grain shear bands in the γ fiber grains. Also, the number of grains that contained in-grain shear bands increased as the deformation temperature was lowered within the warm rolling temperature range. The formation of in-grain shear bands was not observed during deformation under medium or high Z, i.e. at 950 °C or above, in any of the papers since during deformation at 950 °C, DRV was able to overcome the work hardening and no flow localization occurred.

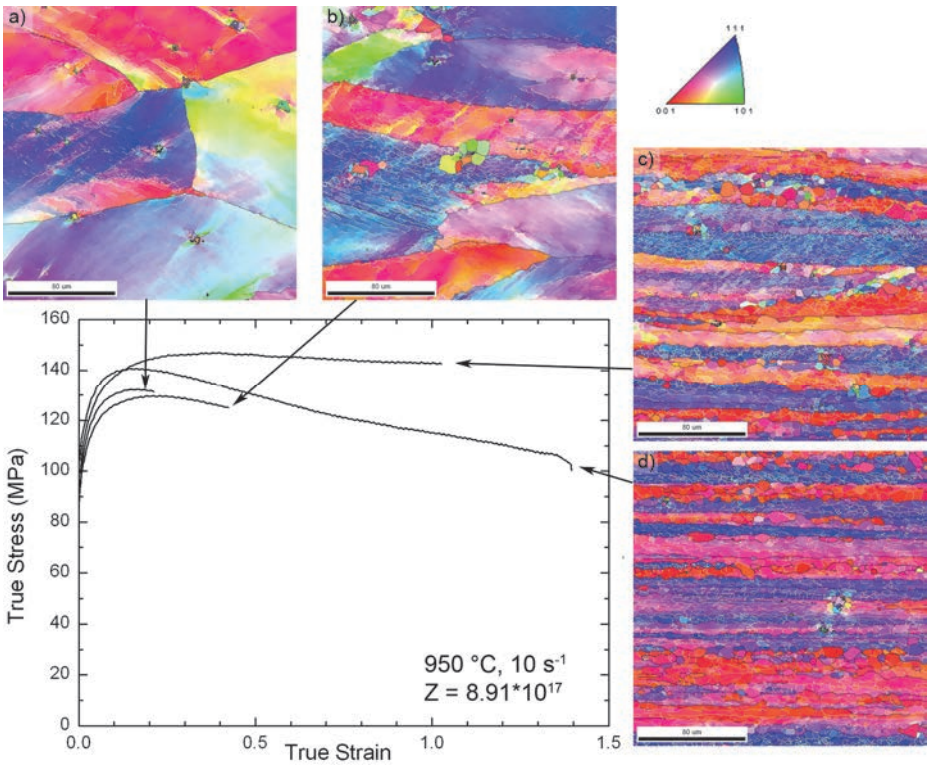

Fig. 15. Flow stress curves and IPF-Z EBSD maps of the dynamically formed microstructures under Z = 8.91 × 10^{17} s^{-1} (950 °C, 10 s^{-1}) after straining to a) 0.2, b) 0.5, c) 1 and d) 1.5. The micron bar is 80 µm long. [Paper III, published by permission of Elsevier Ltd.]

4.3 Static recrystallization

After a hot deformation pass, the microstructure undergoes SRX at high hot deformation temperatures. The effect of deformation conditions on the SRX behavior and kinetics is described in Papers II and V.

4.3.1 Static recrystallization kinetics

The effect of the deformation temperature on the SRX kinetics is presented in Fig. 16 for steel #3, which contains 21% Cr (Paper II). The experimentally achieved values for the statically recrystallized fractions after deformation to the true strain

of 0.4 at 950–1050 °C at 1 s^{-1} fit quite nicely to the sigmoidal shape of the Avrami equation for X_{rex} (Eq. 17). However, the SRX seems to slow down as the SRX process is close to completion, and the last 5% fraction recrystallized more slowly than expected from the Avrami fits, as seen in Fig. 16.

As seen in Table 3, increasing the deformation temperature decreased $t_{0.5}$, which is due to the accelerating effect of the higher soaking temperature on the SRX kinetics. In Paper II the soaking after the deformation pass was carried out at the deformation temperature. Based on this data the value for the apparent activation energy for recrystallization, Q_{app}, was determined to be 221 kJ/mol.

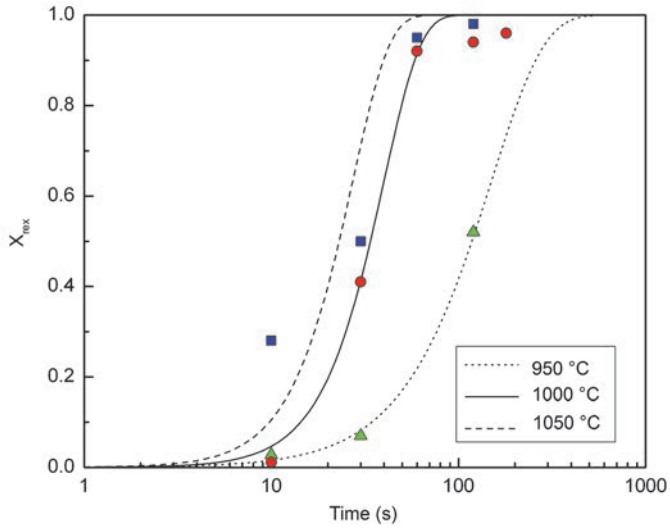

Fig. 16. SRX fractions calculated from the EBSD maps after straining to 0.4 at a strain rate of 1 s^{-1}, and the Avrami fits [Paper II, published by permission of Elsevier Ltd.].

The values for the Avrami exponent, n, (Table 3) provide information about the nucleation mechanisms in the recrystallization event, and, generally speaking, the values of n are independent of the temperature; however, some variation is seen here. The reason for this is not entirely clear, though recovery might contribute to the values.

Table 3. Values of n and $t_{0.5}$ in the Avrami equation for 21%Cr steel (#3) after straining to 0.4 at 950, 1000 and 1050 °C [Paper II, published by permission of Elsevier Ltd.].

Parameter	950 °C	1000 °C	1050 °C
n	1.5	2.2	2.2
$t_{0.5}$ [s]	118	34	21

Increasing the degree of deformation also affected the SRX kinetics as seen in Fig. 17 where the effect of strain on the SRX kinetics at 1000 °C is presented for the 21% Cr steel (#3). Increasing the strain from 0.2 to 0.4 significantly accelerated the SRX kinetics, however, increasing the strain to 0.6 had no further accelerating effect. The value for p, i.e. the strain exponent, in Eq. 18 was determined to be −1.7 over the strain range 0.2–0.4.

The deformation temperature had a significant effect on the SRX kinetics, as observed in Paper V, where the specimens were quenched after the deformation and re-heated for annealing at 950 °C for 30 s. Lowering the deformation temperature to below the conventional hot deformation temperature range significantly accelerated the SRX kinetics during annealing at 950 °C. The deformation was carried out at 1 s^{-1} to the true strain of 0.5 using plane strain deformation, and the deformation temperature range investigated was 550–950 °C. After deformation at 950 °C and annealing, only a few recrystallized grains were formed, while the total recrystallized fraction remained very low, ~1%. However, lowering the deformation temperature to 800 °C and 750 °C increased the SRX kinetics, and similar 30 s soaking at 950 °C led to recrystallized fractions of 87% and 90%, respectively. After deformation at 550 and 600 °C, the same soaking procedure at 950 °C led to complete SRX within 30 s as seen in Fig. 18.

The accelerating effect of lowering the deformation temperature on the SRX kinetics was caused by less efficient DRV at the lower temperatures, and the formation of in-grain shear bands, which offered suitable nucleation sites for the nucleation of SRX. During deformation at 950 °C, DRV reduced the stored energy of deformation, i.e. the driving force for SRX. Also, no in-grain shear bands were formed.

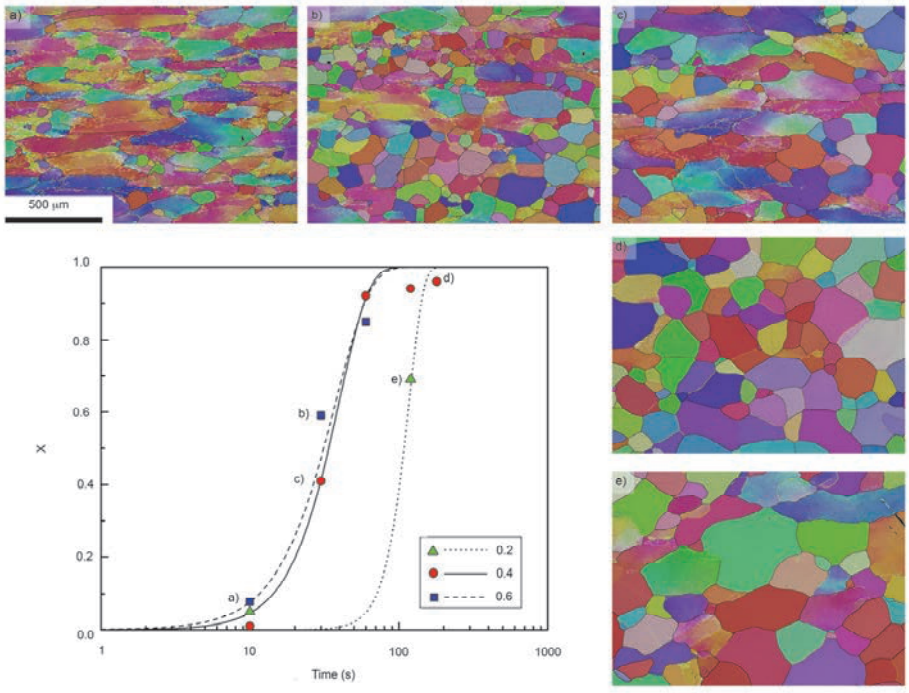

Fig. 17. The effect of strain on the SRX rate at 1 s^{-1} at 1000 °C, and the corresponding SEM-EBSD maps of the partly recrystallized microstructures at 1000 °C: a) 0.6 strain, 10 s holding, b) 0.6 strain, 30 s holding, c) 0.4 strain, 30 s holding, d) 0.4 strain, 180 s holding and e) 0.2 strain, 120 s holding. [Paper II, published by permission of Elsevier Ltd.]

4.3.2 Microstructure evolution during static recrystallization

SRX nucleated first at the original grain boundaries – especially at the triple junctions and in the in-grain shear bands, if present in the deformed microstructure. The number of recrystallizing grains increased when the deformation conditions were altered so as not to be favorable for DRV, i.e. increasing the Z. Also, increasing the degree of deformation from 0.2 to 0.4 led to an increase in the number of recrystallizing grains, which was due to higher amount of stored energy in the microstructure as a result of a higher degree of deformation. However, further increasing the degree of deformation did not accelerate the SRX kinetics.

The SRX grain size depended on the deformation conditions and strain, as seen in Fig. 17. However, regardless of the deformation conditions, the grain-refining effect of SRX was small in Paper II. After deformation at conventional hot deformation temperature of 1000 °C to strains of 0.4–0.6, SRX led to little or no grain refinement, and as seen in Fig. 17, and after straining to 0.2 and soaking for 120 s, some of the recrystallized grains grew even larger than the initial grain size.

In Paper V grain refinement was achieved by lowering the deformation temperature as seen in Fig. 18. The measured SRX grain size after deformation in the conventional hot deformation temperature of 950 °C was 85 μm; however, after deformation at 750–550 °C the SRX grain size was measured to be 21–22 μm. The grain refinement was attributed to the in-grain shear bands, which offered a great number of suitable nucleation sites for SRX, so that nucleation took place not only at the original grain boundaries but also within the deformed grains.

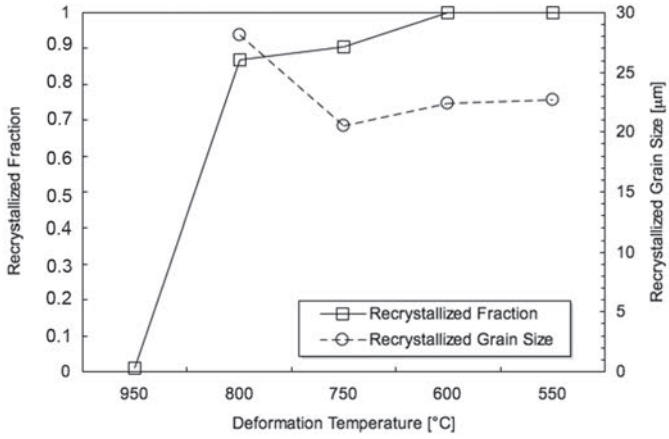

Fig. 18. Recrystallized fraction and grain size after annealing at 950 °C for 30 s as a function of the deformation temperature. The deformation was carried out to the true strain of 0.5 at 1 s^{-1}. [Paper V, published by permission of Trans Tech Publications Inc.].

4.4 Texture evolution

The deformation behavior of a grain depends greatly on its orientation. During hot deformation in conventional industrial hot deformation conditions, ferritic stainless steels develop a strong α fiber texture (<110>//RD), which is generally considered to be the deformation texture fiber, and more or less weak γ fiber (<111>//ND). Also, in most cases there is an additional intensity maximum at the beginning of the ε fiber at <001>{110}. This typical hot deformation texture is not optimal considering the deep drawability of the final cold rolled and annealed sheet.

4.4.1 Deformation textures

Deformation textures were investigated in Papers III–V. The typical hot deformation texture fibers, α, γ and ε, were present regardless of the deformation conditions, however, the locations of the individual texture intensity maxima varied as a function of the deformation conditions.

When using strain rate of 1 s^{-1}, which is relatively low compared to the strain rates in the industrial hot rolling, lowering of the deformation temperature from 950 °C to 800 °C and 750 °C, led to the weakening of the intensity of the α fiber, and the intensity maximum along the α fiber was shifted from the beginning {001}<110> to the end {112}<110>. After deformation at even lower temperatures of 550 °C and 600 °C, the texture intensity maxima were detected at the beginning of the α fiber at {001}<110> and between {112}<110> and {113}<110> as seen in Fig. 19. Also the γ fiber was intensified compared to the deformation textures formed at 750 °C or above.

The effect of the third, i.e. the final, pass temperature of the simulated Steckel mill rolling on the deformation textures was investigated in Paper IV. The strain applied in the final pass was 0.45 using strain rate of 20 s^{-1}. The deformation temperature of the third pass was varied between 950 °C and 650 °C, and the cooling rate from 650 °C to room temperature between water quenching and slow controlled cooling.

Unlike in Paper V, in Paper IV, neither the deformation temperature nor the cooling rate had a significant effect on the macroscopic deformation textures, as is shown in Fig. 20. After the third pass, regardless of the deformation temperature, both α and γ fiber were present as well as a maximum at the beginning of the ε fiber at {001}<110>. The effect of the deformation conditions,

i.e. Z, on the texture evolution was investigated as a function of strain in Paper III. It was evident that Z and the dynamic restoration mechanisms affected the texture structures; however, the deformation textures were in all cases rather typical of BCC materials. After straining to 0.2, the texture structures were still quite random as in the initial transfer bar after solution annealing. However, when the straining was continued to higher strains, the conventional α and γ fibers intensified. Their relative intensities and the locations of the individual intensity maxima varied as a function of the deformation conditions.

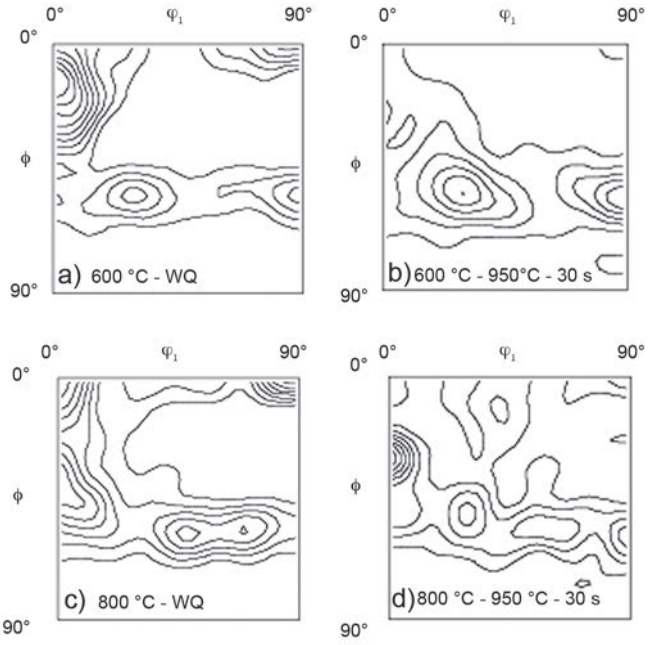

Fig. 19. The $\varphi_2 = 45°$ cross-sections of the ODFs of specimens deformed at a) and b) 600 °C and c) and d) 950 °C. a) and c) represent deformation textures and were measured of water-quenched specimens while b) and d) were soaked at 950 °C for 30 s and are therefore annealing textures. [Paper V, published by permission of Trans Tech Publications Inc.]

Under the lowest Z, CDRX was operating, and after straining to the highest strain of 1.5 the γ fiber became extremely weak, whereas the α fiber was significantly intensified. However, after deformation under higher Z, all the conventional fiber textures, α, γ and ε at {001}<110>, were present. Furthermore, regardless of Z,

there was always an intensity maximum at the beginning of the ε fiber at {001}<110>.

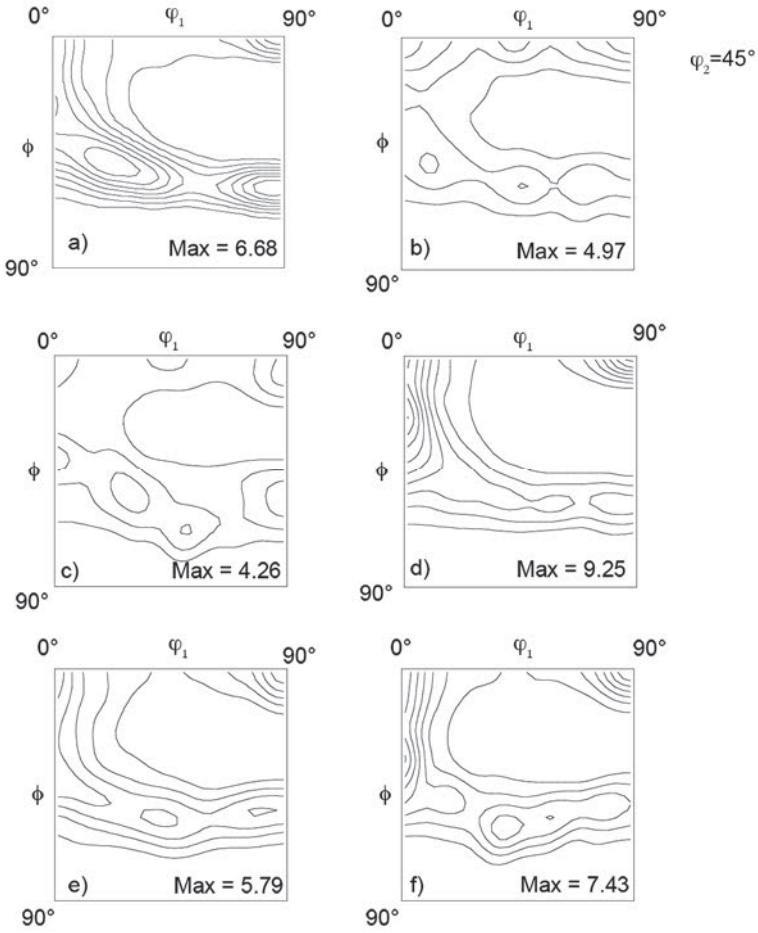

Fig. 20. φ_2 = 45° cross sections of ODFs: a) 950 °C + WQ, b) 950 °C + slow cooling, c) 800 °C + WQ, d) 800 °C + slow cooling, e) 650 °C + WQ and f) 650 °C + slow cooling. [Paper IV, published by permission of The Iron and Steel Institute of Japan]

4.4.2 Annealing textures

The differences in the deformation textures affected the texture formation during SRX i.e. the formation of annealing textures. In Paper V, after deformation using

a rather slow strain rate of 1 s^{-1} at 600 °C or 550 °C and recrystallization annealing, an intensified γ fiber was formed while the α fiber was rather weak, which can be considered beneficial regarding the deep drawability of the end product. The favorable texture development was attributed to the formation of in-grain shear bands in the γ fiber grains, which enhanced the nucleation of γ fiber grains during SRX. No formation of Goss grains was detected during SRX.

The annealing textures formed during soaking after deformation at 750, 800 or 950 °C differed significantly to the ones formed after deformation at 600 or 550 °C. SRX, although not complete but being over 80% after deformation at 750 and 800 °C, did not lead to such positive texture development as with after deformation at 600 °C or 550 °C, and the α fiber was the predominant texture fiber even after SRX. The presence of the α fiber might have been caused by the remaining unrecrystallized grains, which were mainly of α fiber orientations. The occurrence of unrecrystallized grains was caused by the lower number of grains containing in-grain shear bands at 750 and 800 °C compared to 550 and 600 °C, which led to a lower total number of suitable nucleation sites for SRX in the in-grain shear bands, than after deformation at 550 °C or 600 °C. Instead of nucleating in the in-grain shear bands, the SRX grains were formed at the original grain boundaries and, therefore, might also have been of α fiber orientations since the parenting grains could have belonged to the α fiber. In the specimen deformed at 950 °C, only single SRX grains had formed, and the steel underwent mainly SRV during annealing, which explains the high intensity of the α fiber.

4.4.3 Effect of grain orientation on the dynamic and static microstructure evolution

It was seen in Papers IV and V that the number of LAGBs varied significantly between grains with different orientations. Generally speaking, the γ fiber grains contained numerous LAGBs, which were often aligned approximately in a 35° angle relative to the rolling direction, and after deformation at 800 °C or lower, these aligned boundaries became more severe and their misorientation increased, i.e. they became in-grain shear bands. The in-grain shear bands were never observed in the α fiber grains, in which the LAGBs were fewer than in the grains belonging to the γ fiber, and often aligned parallel to the rolling direction.

In Paper V, the deformed grains were divided into two categories based on their morphology and orientation; however, similar classification could have been applied to every Paper except for Paper I, which did not contain microstructure

investigations. Type A grains represent the α fiber (<110>//RD) grains, which contained significantly less LAGBs than type B grains, i.e. the γ fiber (<111>//ND) grains. Also the LAGB structure had different distinctive features in both A and B grain types as presented in Table 4.

Table 4. Identified grain types in deformed structures.

Grain type	Grain morphology	LAGB structure	Orientation
A	Elongated, deformed/recovered	Intermediate amount of LAGBs often aligned along the RD	α fiber (<110>//RD)
B	Elongated, deformed/recovered	High number of LAGBs at a ~35° angle to RD, formation of in-grain shear bands at 800 °C or below	γ fiber (<111>//ND)

The LAGB structure and the SRX kinetics of the α and γ fiber grains differed greatly from each other. Due to the higher dislocation density, the γ fiber grains were the first to recrystallize, whereas α fiber grains were prone to undergo only recovery. Also, the formation of in-grain shear bands in the γ fiber grains enhanced the SRX in the type B grains.

4.5 The behavior of high-Cr ferritic stainless steels in multi-pass hot deformation

The microstructure evolution during multi-pass deformation was investigated in Paper IV by simulating Steckel mill hot rolling on a TMC machine, where the deformation parameters could be selected close to those of the actual Steckel mill rolling. The measured flow stress curves during multi-pass deformation are presented in Fig. 21. True stress represents the measured flow stress, and isothermal stress shows the flow stress compensated for deformation heating as in Ref. [98].

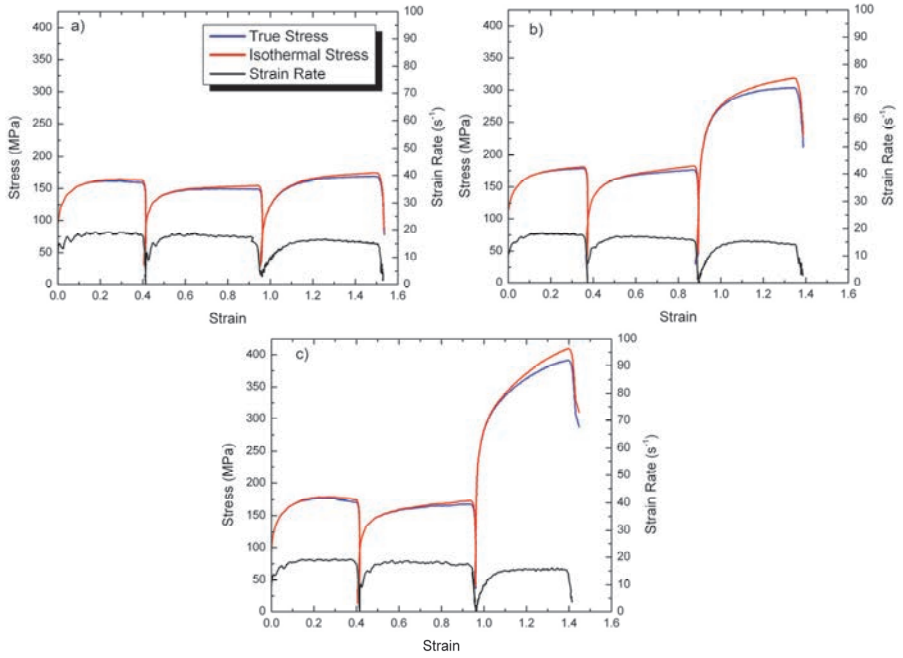

Fig. 21. Stress–strain curves and measured strain rates during three-pass deformation. The first two passes were carried out at 950 °C and the third pass at a) 950 °C, b) 800 °C and c) 650 °C. Blue lines represent the measured true stress, red lines the true stress corrected for adiabatic heating effects and black lines the strain rate. [Paper IV, published by permission of The Iron and Steel Institute of Japan]

4.5.1 Microstructure and texture evolution

Deformation passes at 950 °C (20 s^{-1}, $\varepsilon = 0.4–0.5$) were performed in the DRV region as evident from the LAGBs structure formed during deformation (Fig. 22). As seen in Fig. 21, the flow stress of each pass was at the same level, namely 160 MPa, which indicates that static softening processes during the 20 s inter-pass time led to the complete softening of the material. However, the microstructure investigations revealed that the recrystallization was not entirely complete during the inter-pass period, although the recrystallized fraction was above 90%. In every specimen investigated only a small fraction of the grains underwent recovery as seen in Figs. 22b) and d), and these recovered grains had α fiber orientations. SRX was able to nucleate with the assistance of PSN during the 0.4 s delay between the deformation pass and quench, and the SRX grains are indicated

with white arrows in Figs. 22a) and c). The grain types A and B were present after the first and second deformation passes and are indicated with letters A and B in Fig. 22a).

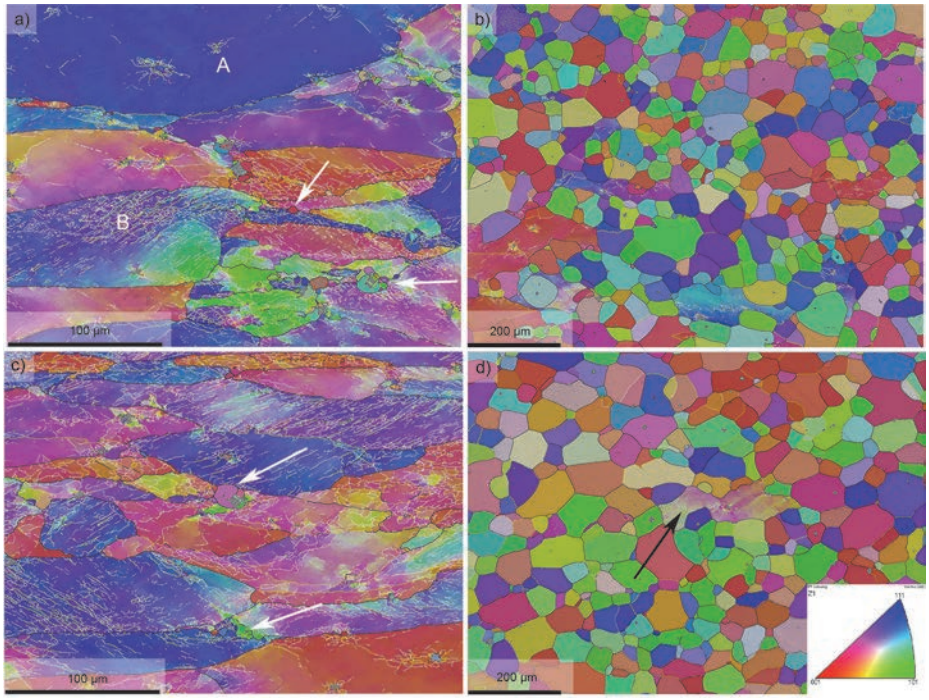

Fig. 22. The microstructure evolution during first two passes (a) and c), respectively) and inter-pass times (b) and d), respectively) of simulated Steckel mill rolling. The grain types A and B are identified in a). In d), a recovered grain is indicated with a black arrow. Arrows in a) and c) indicate small SRX grains. [Paper IV, published by permission of The Iron and Steel Institute of Japan]

The SRX during the first inter-pass period reduced the grain size from 72 µm to 39 µm, and after the second inter-pass period the measured grain size was 54 µm. However, the recrystallized fraction was marginally higher (97%) than after the first inter-pass period (92%). Otherwise, the recrystallized structures are similar after the first and second inter-pass times.

The texture development during the first two passes and the inter-pass times are presented in the $\varphi_2 = 45°$ sections of ODFs Fig. 23. It can be seen that the typical α and γ fiber textures are intensified during deformation and randomized by the recrystallization during the inter-pass period. After the first pass, the

intensity maxima are located at {223}<110> and {001}<110>, and also along the γ fiber at {111}<132> and {111}<011>. Similarly, after the second pass, the intensity maxima are located along α and γ fibers at {001}<110> and {111}<011>. Even though inter-pass SRX randomized the texture, the α and γ fibers remain visible as seen in Fig. 23.

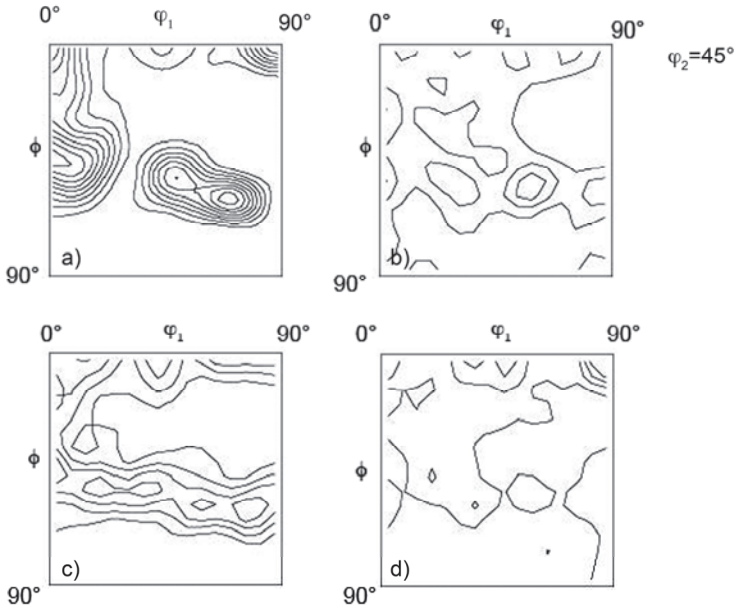

Fig. 23. ODFs after a) first pass + WQ, b) first pass and 20 s inter-pass time, c) second pass + WQ and d) second pass and 20 s inter-pass time. The contour lines represent intensities of 1, 2, 3 etc. [Paper IV, published by permission of The Iron and Steel Institute of Japan]

4.5.2 Effect of the third pass temperature on microstructure, texture and dislocation structure

As the deformation temperature was lowered from 950 °C to 800 °C and further to 650 °C, the dislocation storage in the microstructure was increased as a result of less effective DRV, which was seen as an increased number of LAGBs. The microstructures, which were formed at 800 °C and 650 °C, contained features associated with cold deformation, i.e. there was no obvious effect of DRV and a banded structure within the grains. As was found in Paper V, using a strain rate of

1 s^{-1}, in-grain shear bands were formed at 800 °C and especially at 650 °C, but not at 950 °C. Minor recovery occurred during the slow cooling regimen from 650 °C to room temperature, as seen in the dislocation structures presented in Fig. 24.

In addition to types A and B, a third type of grain, type C, was also detected. Type C grains formed through SRX between the second and the third pass or statically during the 0.4 s delay between the deformation pass and quench, i.e. after the third pass when the pass was carried out at 950 °C. Therefore, some type C grains contained substructure whereas others did not. Furthermore, type C grains were of random orientations. These three types of grains were present in every specimen after the third pass.

The third pass temperature had no significant effect on the deformation textures as seen in Fig. 20, and the ODF cross-sections look very similar regardless of the deformation temperature and the cooling rate.

Dislocation structures were affected by the deformation temperature, as seen in Fig. 24, in which typical TEM bright field images of the dislocation structures are presented. At 950 °C, the dislocation structures had undergone DRV, and the overall dislocation density was relatively low, although it varied between the grains. Because of the easy annihilation of dislocations during deformation, the number of dislocations in dislocation tangles was low. The less effective DRV at lower deformation temperatures affected the dislocation structures. At 800 °C, dislocations tangles were formed adjacent to the grain boundaries and some subgrains were also formed. The highest dislocation densities were in the specimen deformed at 650 °C since DRV had not taken place, which is in accordance with the high amount of work hardening observed in the flow stress curves (Fig. 21). Numerous dislocations were in tangles forming cell walls, and there was also a high number of dislocations within the cells.

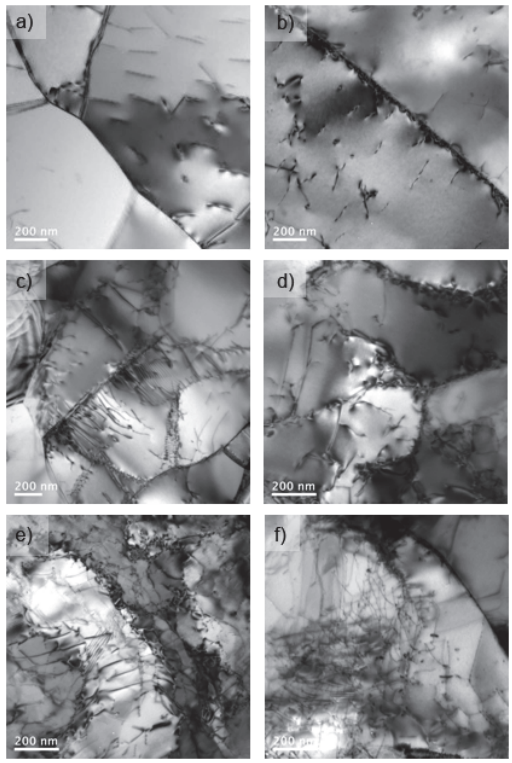

Fig. 24. The effect of the 3rd pass temperature and cooling rate on the dislocation structures in specimens deformed at a) and b) 950 °C, c) and d) 800 °C and e) and f) 650 °C. Specimens a), C and e) were water quenched after the deformation, whereas b) and d) were water quenched to 650 °C and then slow cooled to room temperature. Specimen f) was slow cooled to room temperature. [Paper IV, published by permission of The Iron and Steel Institute of Japan]

5 Discussion

5.1 Interpretation of the activation energy of hot deformation

The values of Q_{def} for steels with 12 to 27 wt.% Cr were determined in Paper I. Regardless of the statistical insignificance of the calculated Q_{def} values, it was found that Q_{def} decreased with increasing Cr content from 359 kJ/mol to 329 kJ/mol, while the Cr content changed from 12% to 27%.

The experimentally determined values for the apparent activation energy of hot deformation of ferrite are quite scattered in the literature. The present values of 329–359 kJ/mol are slightly lower than the previously determined value of 375 kJ/mol for AISI 430 (0.05% C, 16.65% Cr) in the dual phase region [12], 385 kJ/mol for a high purity 17% Cr ferritic stainless steel [99] or 372 kJ/mol for Ti containing IF steel deformed in the ferrite region [100]. However, some even lower values have previously been reported; e.g. 315 kJ/mol for 17% Cr ferritic stainless steel [101] and 280 kJ/mol for ferritic iron [11].

All of these values are significantly higher than the Q_{diff} of pure iron, which has been determined to be 239 kJ/mol [95]. However, as stated in [26, 30, 32] the Q_{def} values, that are determined based on the empirical hyperbolic sine equation, can be significantly higher than the activation energy for lattice diffusion. Furthermore, in the incidence of power law break-down, the activation energies determined for creep can differ markedly from the values of lattice diffusion activation energy – perhaps due to the temperature dependency of the shear modulus [26], which might also affect the Q_{def} values determined for hot deformation, causing them to be significantly larger than Q_{diff}. Nevertheless, the value for Q_{diff} is often given as a reference.

The reason for the apparent decrease of Q_{def} with increasing Cr content is not clear. Cr can alter the SFE, which would affect the extent of dissociation of dislocations, thereby affecting the ability of dislocation cross-slip. In creep, the occurrence of cross-slip decreases the Q_{cr} [27]. However, the current observation differs from the earlier observations of Medina and Hernandez [102] who reported that most alloying elements, except for C, have an increasing effect on Q_{def}. However, Medina and Hernandez [102] investigated the effect of alloying on Q_{def} for low alloy and microalloyed steels in the austenitic state.

Increasing the Cr content from 12 to 27% is also likely to change the phase equilibrium of various precipitates, hence having an effect on the number and

composition of precipitates or the amount of other alloying elements in solution. Also, since the value of Q_{def} has been found to be sensitive even to small alterations in the composition of the steel [102], the fact that Cr content affected the Q_{def} is in line with the previous results.

Nevertheless, great care should be taken when analyzing the experimentally achieved values of Q_{def} and especially the phenomena affecting them, since, in the end, the calculated Q_{def} values based on the empirical hyperbolic sine equation really just describe the dependence of the flow stress on the deformation temperature: the higher the value of Q_{def}, the higher the temperature dependence. Due to the employment of an empirical equation for Q_{def} determination, the calculated Q_{def} should be taken as an *apparent* value and, therefore, Q_{def} is not necessarily related to any single underlying physical phenomena.

5.2 Evaluation of the developed flow stress models

The flow stress models were developed and presented in Papers I and II. The first model was purely empirical and was based on the Arrhenius-type hyperbolic sine equation (Eq. 8). In Paper II, it was employed only for the 21% Cr containing steel (#3). The second model was based on Bergström's equation, which is a physical equation taking into account the variations in the dislocation density as a function of strain. In order to apply the model for steels with various Cr contents, two additional empirical equations were developed, and the complete model was therefore a combination of physical and empirical equations.

Both models were successfully fitted to the flow stress curves, as seen in Figs. 5 and 6. The Pearson's correlation coefficient between the experimental and calculated flow stress values was 0.995 for the empirical model and 0.990 for the physical-empirical model, and therefore, both fits can be regarded as successful.

The main drawback with empirical models is that they are only applicable to those deformation conditions, for which they were developed. Outside the range of those parameters, the suitability of the model for flow stress prediction cannot be guaranteed. However, they work very well in the range used for model development. The empirical equations do not take into consideration the actual physical phenomena behind the observed flow stress values. However, it may not be a negative issue if the model is capable of accurate flow stress predictions. On the other hand, the physical phenomena that take place during hot deformation are quite complex, and the measured flow stress is not only a result of the formation and annihilation of dislocations but also deformation induced precipitation or

dislocation–precipitate interactions. These phenomena are rather difficult to predict, let alone to describe mathematically.

By using the currently developed physical-empirical equation, the flow stress curves were successfully calculated for steels containing 12–27% Cr, as seen in Fig. 6. The model led to overshooting of the calculated flow stress only for certain individual flow curves, and the overall correlation between the experimental and calculated values was very good. Furthermore, the shape of the calculated flow curves corresponds to the experimental flow curves, as seen in Fig. 6.

In addition to Pearson's correlation coefficient value, the success of the developed model, which combines the Bergström's equation to two empirical equations, was evaluated by calculating the values for dislocation density by using Eq. 13 and the predicted values for Ω and U (Eqs. 16 and 21). The square root of the calculated dislocation density had a corresponding linear dependency to the measured flow stress, as seen in Fig. 12. According to Bergström [38], the initial dislocation density of well-annealed ferrite is 2.0×10^{12} m^{-2}, and after a couple of percent deformation at ambient temperature the dislocation density increases to 10^{14} m^{-2}. The lowest dislocation density calculated in the current investigation was 2.13×10^{12} m^{-2}, which seems reasonable compared to the values given by Bergström [38]. However, the highest value, 1×10^{14} m^{-2}, seems quite high and corresponds more to the dislocation densities achieved in cold deformation. However, calculating dislocation densities was not the purpose of the model, but rather being able to fit the calculated flow curves to the experimental ones for a range of different Cr contents, which was achieved.

In Paper II, the conventional application of the Arrhenius hyperbolic sine equation was found not to be suitable, since the flow stress did not achieve a steady state under every Z and nor was a peak stress detected. Therefore the flow stress analysis was carried out at strain intervals of 0.1, 0.15, 0.2, 0.25, 0.3 and 0.35. At each value of strain, flow curves are at different stages of deformation and may be subjected to different deformation or softening mechanisms. Therefore, strain was incorporated into the constitutive equations, as in [91–94, 99]. Good overall results were achieved, and deviations between the experimental and calculated flow stress values occurred only during the highest strain rate deformation. Therefore, it can be concluded that some further development of the model could have been carried out, perhaps by adding a strain rate exponent in the equation for Zener-Hollomon parameter (Eq. 8), similarly as in Paper I for Z' (Eq. 19) and Z'' (Eq. 20).

Although both modeling approaches led to successful flow curve fits, it is necessary to discuss whether the selection of the flow stress model used in Papers I and II was justified. The flow curves for the hot deformation of ferritic stainless steels are smooth, and a well-defined peak stress or undulations do not occur, i.e. the flow behavior is representative of DRV. Therefore, the flow stress model would not need to be able to take into account the effect of DRX on flow behavior. The Arrhenius equation-based hyperbolic sine equation is probably the most commonly used empirical equation for hot deformation flow behavior. It is also rather simple and easy to apply. Due to these facts, there is plenty of literature with which to compare the results, and therefore it is a good choice for a starting point for flow curve analysis.

Bergström's equation, on the other hand, might not be the most widely used model; however, among the physical models for hot deformation, it is a quite simple one, and does not contain a great number of materials constants, which would be difficult to calculate or measure accurately. Bergström's model is not necessarily the most sophisticated model compared to, for instance, a more recent model by Roters *et al.* [39]; however, it was chosen due to its simplicity and suitability for modeling DRV controlled flow.

Bergström proposed the model for α-iron [38], but due to the austenite–ferrite phase transformation in α-iron, the deformation was carried out at a significantly lower temperature than in the current investigation in order to stay in the ferrite region, i.e. ambient temperature to 630 °C. The Bergström's model has been employed previously for low plain C steels at 700 °C [103] and at 900–1200 °C, i.e. in the austenitic state [104], for predicting tensile stress–strain curves for dual-phase steels at room temperature [105] and for magnesium alloys at 200–400 °C [106], but not for Cr-alloyed ferritic stainless steels in the hot deformation temperature range.

5.3 Flow stress curves and the dynamic restoration mechanisms

The flow curves of the current investigation were typical for DRV controlled flow, and the microstructures were indeed mainly dynamically recovered. However, dynamically formed grains were detected in the microstructure without any indication of DRX in the flow curves, which might be caused by the low overall recrystallized fraction. However, there is mixed information in the literature about the effect of CDRX and other DRX mechanisms on the flow behavior of ferrite.

According to the classic study by Glover and Sellars [11], DRX in α-iron under low Z causes multiple undulations in the flow curve, whereas under high Z when DRV occurs, the flow curves were smooth and no decrease of the flow stress is detected. However, DRX can also cause a single smooth peak, after which the flow stress decreases and reaches a steady-state value in the flow curves. According to Desrayaud *et al.* [45], the oscillations have always been associated with DDRX in high SFE metals, but they never occur during CDRX or during DDRX under high Z, which results in a single peak behavior, although the shape of the peak is different from that of CDRX, which is much smoother than the DDRX peak [45].

Indeed, a smooth single peak behavior has been reported when CDRX has occurred in AISI 430 ferritic stainless steel [65], in a microalloyed steel during deformation in the ferrite region [69], or in an 11% Nb-Ti stabilized ferritic stainless steel [64]. However, it has also been reported that the flow stress can reach a steady state and that no decrease occurs during CDRX in a 26% Cr ferritic stainless steel [16] and during deformation in the ferrite region of an IF steel [66] and a low C steel [67], which is in accordance with the current results. Therefore, no conclusions of the occurrence of any DRX mechanisms could be drawn based on flow curve analysis.

5.4 The effect of Zener-Hollomon parameter on the dynamic restoration mechanisms

The microstructure and especially the subgrain structure were greatly dependent on Z. The results in Paper III confirmed the earlier results in ferritic stainless steels by Gao *et al.* [16], who concluded that during steady state flow, a constant subgrain size is maintained by the interaction between dislocations in sub-boundaries, and the subgrain size has been noted to increase with decreasing Z.

The dislocation structures were also greatly affected by Z, as presented in Papers III and IV. At 950 °C, the dislocations were more numerous than at 1050 °C due to less efficient DRV and annihilation of dislocations, which is in line with what has been previously presented in the literature [16], and no exceptional dislocation structures were discovered.

According to the classic work of Glover and Sellars [11] on vacuum-melted and zone-refined iron, the restoration mechanism shifts from mainly DRV under high Z to DRX under low Z deformation, i.e. when the deformation temperature is increased and/or strain rate is decreased. The change occurs at $Z = 1 \times 10^{12}$ s^{-1}

for vacuum-melted iron and at $Z = 1 \times 10^{15}$ s^{-1} for zone-refined iron [11]. The difference is caused by differences in the purity levels, i.e. the amount of C and N in solution [11]. However, different values for the critical Z have also been reported: e.g. Longfei *et al.* [46] concluded that the change took place at $Z = 10^{16}$ s^{-1} in low-C steel in the ferrite rolling temperature range of 550 to 700 °C.

According to Glover and Sellar's study [11], the change in the restoration mechanisms should be visible in the flow stress values when plotted against Z. In the DRV region, the relationship between the steady state stress and Z should be exponential whereas, when DRX occurs, the steady state stress should have a power relationship with Z [11]. The average flow stress was plotted as a function of *ln Z* in Fig. 7, in which a linear line was fitted successfully over the whole stress range on a *ln Z* scale, which indicates an exponential relationship between Z and flow stress. Contrary to the study by Glover and Sellars [11], a change from an exponential to a power relationship did not occur in the currently investigated steel, and the occurrence of DRV was able explain the flow stress values under every Z. However, in the current study only four different deformation conditions were applied, and more tests under wider range of Z should be carried out in order to verify the result.

A similar change in the dynamic restoration mechanisms to that proposed by Glover and Sellars [11] has also been reported to occur in 26% Cr ferritic stainless steel by Gao *et al.* [16]. Their observations of the substructure development during hot deformation are very similar to the observations presented in Paper III. In both studies, the main restoration mechanism was DRV under high Z, whereas under medium or low Z, DRX took place, and the resulting grain sizes were a function of Z, (Fig. 14) being coarsest under the lowest Z. However, the exact values for Z cannot be compared between the two studies, since Gao *et al.* [16] did not state the exact values for Z and only referred to them as being "high", "medium" or "low". Further, they did not state what the exact DRX mechanism was that they observed under low and medium Z deformation, but they described it as occurring by rotation of subgrains and coalescence of subgrain boundaries, i.e. CDRX.

The differences in the deformation temperature make comparing the current results with the literature rather difficult, since investigations into DRX of ferrite in the hot deformation temperature range are scarce. Most studies on DRX in ferrite e.g. [11, 53, 107], have been carried out in the ferrite range, i.e. below 850 °C or so. Only the investigations by Gao *et al.* [16] on a 26% ferritic stainless steel and by Oliveira and Montheillet [64] on a Ti-Nb stabilized 11% and 17% Cr

ferritic stainless steels were carried out at high hot deformation temperatures. The difference in the deformation temperature very likely affects the restoration mechanisms and the conclusions that were drawn after deformation below 850 °C may not be applicable to hot deformation at 950–1050 °C.

Glover and Sellars [11] stated that DRX should only occur under low Z, i.e. at high temperatures and low strain rates. However, in the current investigation, under the lowest Z, the observations indicate that DRV is very intensive and therefore, the amount of stored energy is likely to remain under the required critical value for the nucleation of DDRX. In other words, it is unlikely that the driving force for DDRX would be sufficient under low Z deformation.

However, based on the microstructural observations in Paper III, DRX under medium Z ($Z = 4.67 \times 10^{16}$ s^{-1}), i.e. at high strain rate and high temperature, seems more likely. Due to the high strain rate, dislocations are piled up increasing the stored energy, and the high deformation temperature of 1050 °C might allow DDRX to nucleate. New grains were observed at the original grain boundaries as a "necklace" type of structure in the specimen deformed under $Z = 4.67 \times 10^{16}$ s^{-1} (i.e. 1050 °C, 10 s^{-1}), which were similar to grains which would have formed as a result of SRX or DDRX. However, it was not possible to verity the nucleation mechanism due to the delay period before quenching. Under the highest Z ($Z = 8.91 \times 10^{17}$ s^{-1}), the initiation of the occurrence of GDRX after straining to 1 or 1.5 cannot be ruled out. Especially after straining to 1.5, the original grains were heavily flattened and pinching off of new grains seemed to have occurred.

In addition to the deformation conditions, the purity of material affects the occurrence of DDRX [11, 53], since small precipitates, which pin the boundaries, may prohibit the occurrence of DDRX. However, removing the C and N from solution by alloying the steel with stabilizing elements may enable the occurrence of DDRX also in high SFE metals as presented for IF steels in [53]. The steel investigated (#6) was industrially produced and, therefore, contained relatively high amounts of impurities. Although the steel was alloyed with stabilizers Ti and Nb, which are strong carbide and nitride formers, some C and N are still likely to have remained in solution, thereby prohibiting the occurrence of DDRX. Therefore, if a very high level of purity is required for the occurrence of DDRX in high SFE metals, the occurrence of DDRX seems unlikely in the currently investigated steel. However, as stated earlier, the 0.4 s delay period between the deformation and the quench would have allowed SRX to nucleate, and therefore prohibited the verification of the occurrence of DDRX or any other DRX mechanism.

5.5 Effect of dynamic restoration mechanisms on texture

Only DRV and CDRX occurred in the current investigation to the extent that their effect on the deformation texture could be defined. However, their effects are rather similar since CDRX is a DRV based process and neither of the processes causes nucleation of new grains. Therefore, the changes they cause in the texture formation are rather subtle. However, the movement LAGBs and HAGBs, which are essential features of CDRX, can greatly depend on the grain orientation and are affected by precipitate pinning and selective particle drag [80]. Therefore, CDRX may affect the formation of deformation textures, even though conventional DRV does not [7]. Indeed, the textures formed during DRV, e.g. in Paper V at 950 °C, were composed of the typical hot deformation texture fibers α, γ and ε at {001}<110>.

In Paper III the extent of DRV and dynamic recrystallization mechanisms varied as a function of Z, as did the effect of DRV on the deformation textures. Under most Z except for the lowest, the typical deformation texture fibers α, γ and ε had formed. However, after straining to 1.5 and when a steady state flow and microstructure development was achieved as a result of CDRX, the intensity of the α fiber was significantly higher that of the γ fiber, which seemed to have almost disappeared. The intensity maximum was at {001}<110>. Therefore, it can be concluded that, during deformation under low Z and CDRX, grain rotations away from the γ fiber and towards the α fiber orientations had occurred. The theories of oriented nucleation do not apply, since no nucleation of new grains occurred. However, some boundaries might have had an energy advantage and therefore higher mobility compared to others, as in the theory of oriented growth [8]. Also, precipitate pinning and Zener drag might have affected the texture formation as in [80].

However, it is to be noted, that CDRX might also have taken place under higher values of Z together with GDRX in Paper III. Therefore, under medium and high Z, CDRX did not cause significant weakening of the γ fiber as under the lowest Z. Furthermore, the strains applied in Paper III are low compared to the other investigations into CDRX where torsion and significantly higher strains were employed, and not all of the grain rotations which would eventually have occurred had yet taken place in Paper III.

The observations in the literature on the texture development during CDRX are scarce, and they are often achieved in torsion, i.e. they are torsion textures and therefore not totally comparable to texture structures formed under plane strain

deformation. However, Gourdet and Montheillet [59] stated that the textures formed under CDRX are deformation textures, which might be affected by grain boundary migration. The major components should be {112}<110> and {112}<111>. Indeed, the formation of intensity maxima at {112}<111> has been reported in an 11% Cr dual-stabilized ferritic stainless steel under CDRX in torsion [64]. In Paper III, under the lowest Z, the intensity maximum was formed at the beginning of the α fiber at {001}<110> but not at {112}<110> as in the literature. After deformation under medium and high Z, the intensity maximum is located at {112}<110>. Therefore, the current observations are not totally in line with these previous results, but again the previous results in the literature were achieved in torsion and at much higher strains than in Paper III.

5.6 Static recrystallization kinetics

The SRX kinetics is generally strongly dependent on the degree of deformation. However, in Paper II, no accelerating effect on the SRX kinetics was detected between strains 0.4 and 0.6, indicating that no more deformation is stored beyond 0.4 strain at 1000 °C. The power of strain, p, in Eq. 18, between the strains of 0.2 and 0.4 was calculated to be −1.7, which is significantly smaller than values previously proposed for austenitic steels; −3.81…−3.55 [75], −4 [108] and −2.2 [109]. However, the recrystallization behavior of austenite and ferrite differ significantly from each other due to the different SFE. It should also be noted that the values for the strain exponent p for ferritic stainless steels was not to be found in the literature, and it was therefore reported for the first time in Paper II.

The fact that increasing the degree of deformation increases the SRX rate only to a certain limit was also observed in IF steels by Akbari *et al.* [110]. The behavior is likely to be related to the steady state flow stress behavior as observed by Glover and Sellars [10] in α iron. They concluded that, after a steady state is achieved, increasing the degree of deformation does not increase the SRX kinetics any further, i.e. in the steady state region, SRX kinetics is independent of the strain [10]. At low strains, on the contrary, the accelerating effect is very strong [10]. The lack of an accelerating effect of strain could be caused by extensive DRV, which prevents dislocation storage in the microstructure in such a way that increasing strain in the “steady-state” region does not increase the driving force for recrystallization.

Also slowing down of the SRX kinetics was detected towards the completion of the process more than might have been expected from the Avrami fits. This

"sluggish" recrystallization towards the end of the completion of recrystallization has also been reported before by Sinclair *et al.* [17] in AISI 409 ferritic stainless steel during annealing after cold rolling. The effect was caused by heterogeneity in the substructure between various grains, which in turn was caused by precipitates interacting with LAGBs [17]. This type of mechanism could explain the slowing down of the recrystallization rate also observed here, since the LAGB structure was very different from one grain to another.

Also Hinton and Beynon [12] observed two different SRX kinetics for AISI 430 ferritic stainless steel. However, according to their observation, the switch between the kinetics occurred after approximately 70% of recrystallization. Below 70%, the value for n was 2.85, whereas for the recrystallized fraction exceeding 70%, n was 1.03. It is to be noted that Hinton and Beynon [12] investigated the SRX kinetics after hot deformation, whereas Sinclair *et al.* [17] studied the situation after cold rolling. Also, AISI 430 undergoes austenite–ferrite phase transformation, and a banded austenite structure was noted to have affected the SRX kinetics [12].

The cause of the different SRX kinetics has previously been attributed to precipitation, which was interacting with the moving HAGBs of the recrystallizing grains [17, 110]. Precipitation might have retarded the recrystallization kinetics also in the present study, since the steel investigated is highly alloyed with precipitate-forming elements. However, precipitation was not studied in detail within the current investigation and this result cannot therefore be confirmed.

5.7 The effect of lowering the deformation temperature on the microstructure and texture development

Lowering the hot rolling temperature not only increased the stored energy in the microstructure but also led to the formation of in-grain shear bands when the deformation temperature was lowered to 800 °C or below in Papers IV and V. The in-grain shear bands were observed only in the grains belonging to the γ fiber, especially in grains oriented with {111}<110>, which is in line with the literature [15, 20–22]. Evidently, the number of grains, which contained in-grain shear bands, also increased with decreasing deformation temperature.

In Paper V, the deformation temperature significantly affected the formation of deformation textures. As the deformation temperature was lowered, the intensity maximum along the α fiber was shifted from the beginning and middle

of the α fiber closer towards {111}<110>. The in-grain shear bands are known to cause grains to split up, which weakens the texture and slows down the matrix rotations [13–15, 21]. Also, flow localization in the form of in-grain shear bands might prevent grain rotations into the stable and undesirable end orientations of {001}<110> [15]. A similar effect was also observed in Paper V, where lowering of the deformation temperature intensified the γ fiber. The results of Paper V are in line with the previous results by Barnett and Jonas [21], who observed that, during warm rolling of IF and low-C steels in the presence of in-grain shear bands, a partial α fiber and a complete γ fiber are formed. The weakening and of the α fiber has also been observed in 21% Cr ferritic stainless steel when hot rolling finish temperature was reduced to 750 °C [15] and in 17% Cr ferritic stainless steel during rolling at 740–620 °C [14].

Unlike in Paper V, where lowering of the deformation temperature caused clear differences in the deformation and annealing textures, in Paper IV, lowering of the hot deformation temperature from 950 °C to 800 °C and 650 °C, did not cause any clear differences in the deformation textures, as seen in Fig. 20. In both investigations, in-grain shear bands were formed when the deformation temperature was lowered to 800 °C and, therefore, the reason for the different texture development is unclear, but it might be related to the differences in the strain rates. The strain rate applied in Paper V was 1 s^{-1}, whereas in paper IV it was 20 s^{-1}. Also, the dimensions of the plane strain specimens were different as in Paper V, Gleeble plane strain compression tests were employed, while in Paper IV, the test method was TMC compression tests. Further, it should be noted that the EBSD equipment used for the texture measurements were different in Papers IV and V, which might have affected the results.

Lowering of the deformation temperature to 800 °C and 650 °C did result in flow localization and the formation of in-grain shear bands, and the number of LAGBs was also significantly higher than after deformation at 950 °C as in Paper V. Therefore it seems evident that, regardless of the lack of clear effect of deformation temperature on texture in Paper IV, lowering of the deformation temperature would still lead to enhanced product properties. This is because SRX would be significantly accelerated during subsequent annealing due to the higher stored energy in the microstructure and enhanced nucleation of SRX due to the presence of in-grain shear bands.

The variations in the deformation texture due to different deformation temperatures clearly affected the formation of recrystallization textures in Paper V. However, the recrystallization texture was not significantly improved even though

in-grain shear bands were introduced to the microstructure after lowering the deformation temperature to 800 and 750 °C. At 950 °C, only 1% of the microstructure was recrystallized after 30 s soaking at 950 °C, and the intensive α fiber after the soaking was caused by the low recrystallized fraction, i.e. the recrystallization texture was essentially the same as the deformation texture. After deformation at 750 and 800 °C and soaking at 950 °C for 30 s, the recrystallized fractions were ~80%, and therefore the remaining 20 % on unrecrystallized grains were predominantly of α and ε fiber grains, which have slower SRX kinetics than the γ fiber grains due to their lower Taylor factor [83]. The unrecrystallized α and ε grains can explain the strong α fiber, which was still present after recrystallization annealing even though favorable nucleation of γ grains in the in-grain shear bands took place.

Many authors have emphasized the importance of in-grain shear bands and nucleation of SRX in the in-grain shear bands on the formation of {111} recrystallization textures e.g. [15, 20–22]. In the previous studies [20, 22, 23] the nucleation of Goss grains in the in-grain shear bands were also detected in the low C steels, if the in-grain shear bands were too severe. However, as in IF steels, no Goss grains were found to have nucleated in Paper V.

Therefore, it can be concluded that nucleation in the in-grain shear bands in stabilized high-Cr ferritic stainless steels leads to a favorable texture development to some extent regardless of the deformation temperature. Also, Gao *et al.* [13, 14] and Zhang *et al.* [15] have previously drawn similar conclusions for 17% Cr and 21% Cr ferritic stainless steels. The results in Paper V clearly indicate that, in order to achieve favorable texture formation and accelerated SRX kinetics, the deformation temperature has to be lowered from the conventional hot deformation temperature range where DRV is very effective.

5.8 Modification of industrial hot rolling schedules

The strain rates in the industrial hot rolling are high, generally at least 10 s^{-1}, whereas the degree of deformation in a single pass can be relatively low, ~0.4 or less. The deformation temperatures vary, but generally speaking they have a decreasing trend during multi-pass hot deformation. According to conventional thinking, the only dynamic restoration mechanism during industrial hot rolling of ferritic stainless steels is DRV [30], whereas DRX of any form should not take place. This was more or less confirmed in the present study based on the results of Papers III–V.

During the simulated multi-pass hot rolling at 950 °C in Paper IV, using a strain rate of 20 s^{-1}, the accumulation of dislocations was not sufficiently high for the nucleation of DDRX due to extensive DRV. However, the strain was too low for the gradual evolution of LAGBs into HAGBS, i.e. for CDRX as well as for the initiation of GDRX. Furthermore, the steel undergoes complete softening during the inter-pass times, and even though SRX would have not been fully completed, SRV ensures the mechanical softening. Both processes consume the stored energy in the microstructure and no accumulation of deformation is left after the inter-pass period.

Since it is unlikely that any form of DRX occurs under the conventional industrial hot rolling conditions, no grain refinement can be achieved during rolling passes. DRV is very effective in reducing the driving force for SRX and therefore some grains, most often belonging to the α fiber, remain unrecrystallized even after a 20 s inter-pass time. The remaining unrecrystallized grains after hot band annealing are known to have a negative effect on the texture development mainly due to their α fiber orientations [80]. Similarly, unrecrystallized grains can remain in the microstructure after cold rolling and the final annealing, in which case they have a detrimental effect on the deep drawability of the end product [9]. Therefore, actions should be carried out in order to ensure that every grain recrystallizes during inter-pass times and during hot band annealing. This can be achieved by increasing the amount of stored energy in the microstructure and the number of suitable nucleation sites for SRX, both of which accelerate SRX.

Based on the current results, it is obvious that the conventional hot rolling schedules do not produce the optimal microstructure and texture regarding the final product properties. The biggest issue seems to be efficient DRV, which is ultimately caused by the high SFE of ferritic stainless steels. Thus, in order to make DRV less feasible or to prevent it, the deformation conditions of hot rolling should be altered so as to be unfavorable for DRV. Since DRV is a thermally activated and requires diffusion, the means for achieving increased dislocation accumulation in the microstructure are reducing the temperature or increasing the strain rate. These measures would hinder DRV and lead to higher dislocation densities, i.e. an increased amount of stored energy, and therefore to a higher driving force for SRX.

In Papers IV and V, lowering the hot deformation temperature to 800 °C was already enough to increase the rate of SRX during annealing. However, lowering the deformation temperature further to approximately 650 °C would have an even

more significant effect on the SRX kinetics and, according to Paper V, it would also result in intensified γ fiber recrystallization texture. Decreased deformation temperature leads, however, to a significant increase in the flow stress, and it is possible that such an increase becomes critical for the hot rolling mill equipment such that, 650 °C might not be achievable in the industrial hot rolling mill. In simulated Steckel mill rolling (Paper IV), the flow stress at 650 °C increased up to almost 400 MPa, while at 950 °C, using the same strain rate, the measured flow stress was 160 MPa. Therefore, it can be concluded based on the results in Paper V that adequate results are achieved using finishing temperatures of 800 °C and below, which are still achievable on the industrial scale and without altering the strain rates or strain of the single passes. Also, when a lower finishing temperature is employed, as in Paper IV, the slab reheating temperatures could be lowered, which would lead to energy savings.

DDRX during a deformation pass would also affect the texture formation and cause nucleation of small, recrystallized grains. The greatest obstacle for DDRX is the intensive DRV, the reduction of the dislocation density which it causes, and the presence of small particles, which pin the moving boundaries of recrystallizing grains. By shortening the inter-pass times, deformation accumulation in the microstructure might be achieved due to incomplete mechanical softening during the inter-pass period. Eventually, the amount of stored energy due to the dislocation accumulation might become larger than the critical value for the nucleation of DDRX, as in the case of IF-steels [107].

Great grain refinement potential has been attributed to CDRX and GDRX during heavy warm deformation of ferrite [72, 111]. Based on the current results, CDRX or GDRX do not have any impairing effect on the texture during high Z deformation, and therefore altering the deformation conditions favorable for CDRX and GDRX, a finer grain size might be achieved and potentially also enhanced deep drawability of the end product, i.e. increasing the strain rate or decreasing the deformation temperature, is likely to be beneficial. For the initiation of these DRX mechanisms, but especially GDRX, the degree of deformation in a single pass should be increased. For the SRX kinetics, increasing the degree of deformation only increased the SRX kinetics in the work hardening stage; however, increasing the degree of deformation in the steady state region would not further accelerate the SRX kinetics. Since the industrial hot rolling takes place in the work hardening region due to the high strain rate, increasing the strain would also be beneficial for accelerating the SRX kinetics.

Furthermore, lowering the hot deformation temperature to the warm rolling range has a potential to broaden the product range. Based on the current results, warm rolling seems suitable for producing stabilized high-Cr ferritic stainless steels. By combining proper heavy warm rolling with short inter-pass times and subsequent hot band annealing is likely to produce thin gauge hot band with good product properties, i.e. strong γ fiber texture and small recrystallized grain size as in IF steel [112, 113], where heavy warm rolling in the upper ferrite region (700–800 °C) and subsequent annealing produced a hot band with good deep drawability. Production of thin gauge hot band of IF and low C steels has also been presented by Zambrano *et al.* [114] and Petrov *et al.* [115].

Producing a high-Cr ferritic stainless steel hot band with good deep drawability indeed seems possible using heavy warm rolling. However, the surface quality, even after pickling, might not be sufficient for many stainless steel applications, which demand high surface quality. If the key criteria for the application is corrosion resistance, and not appearance, e.g. in some industrial applications, rougher surface finish may be adequate. Therefore, it can be assumed, that after pickling, the hot band high Cr ferritic stainless steel would be ready to use in certain applications, in which case the cold rolling would be unnecessary and great energy and cost savings would be achieved. However, lowering the hot deformation temperature into the warm deformation range might cause additional problems such as roll sticking.

Nevertheless, two different methods for improving the conventional hot rolling of ferritic stainless steels are proposed (Table 5). In the *Enhanced SRX* method, SRX during inter-pass times and hot band annealing is promoted as much as possible, whereas the *Warm rolling* procedure refers to the production of thin gauge hot strip. The *Enhanced SRX* is similar to the improved processes for hot rolling of a 21% Cr ferritic stainless steel by Zhang *et al.* [15] and for 17% Cr ferritic stainless steel by Gao *et al.* [13, 14], which all rely on lowering the deformation temperature of the final hot rolling passes.

The *Warm rolling* route was inspired by the results in Paper III, and previous results by Belyakov *et al.* [109] and Sakai *et al.* [72], who investigated heavy warm deformation in the ferrite range. In Paper III, deformation under the highest Z led to the finest subgrain size, and also the dynamically and/or statically formed grains were the finest. Belyakov *et al.* [111] and Sakai *et al.* [72] observed great grain refinement potential of CDRX and GDRX during heavy warm deformation of ferrite, and therefore optimizing the deformation conditions for CDRX and GDRX seems a promising way to refine the grain size already during hot rolling.

Even if this is not achieved, deformation at a lower temperature would lead to increased dislocation density and therefore enhanced SRX kinetics during hot band annealing, ensuring complete SRX during hot band annealing.

Table 5. The proposed enhanced hot rolling procedures for stabilized high-Cr ferritic stainless steels.

Route	Enhanced SRX	Warm rolling
Actions during multi-pass hot rolling	– Increasing ε in a single pass in the work hardening region – Sufficient inter-pass times – Lowering the temperature of the final rolling passes – Hot band annealing at a sufficiently high temperature	– Lowering the deformation temperature to warm rolling range (< 800 °C) – Increasing the ε and ε' – Short inter-pass times – Subsequent hot band annealing
The effects of altering the hot rolling conditions	- Increase in the amount of stored energy in the microstructure and formation of in-grain shear bands during the final passes – Accelerated SRX kinetics during inter-pass times and hot band annealing – Increase in the γ fiber intensity	– Prevention of DRV, increasing dislocation accumulation, formation of in-grain shear bands – Increase in the stored energy and flattening of the original grains, incidence of CDRX and GDRX – Complete SRX during annealing, small SRX grain size and favorable texture structure
Total improvement compared to conventional hot rolling	– Enhanced SRX refines the grain size, and lowering the hot rolling finishing temperature has a positive effect on the texture formation	– Grain size refinement may be achieved already dynamically during the rolling passes. The lower rolling temperatures lead to formation of in-grain shear bands, which accelerate the SRX kinetics and affect the texture formation. – No need for cold rolling
Possible problems	– Possible technological problems relating to lowering the hot deformation temperature, e.g. roll sticking	– Problems relating to rolling technology when applying high strains and strain rates at rather low temperatures. – Inadequate surface finish of the thin gauge hot band after pickling

5.9 Reliability and validity

In order to simulate hot rolling, compression tests were performed in a laboratory environment by employing either a Gleeble thermomechanical simulator or a TMC machine. Therefore, the process parameters and the deformation state differed to that of actual hot rolling. However, the results have been shown to be comparable when the limitations of the simulations are taken into account. In this chapter, some of the issues will be discussed relating to the physical simulations of hot deformation, which might have affected the current results together with some other issues encountered.

Often in compression tests, the process parameters differ significantly from those of the industrial hot rolling, the greatest difference being in the strain rate. In Gleeble simulations, the strain rates employed varied from 0.01 s^{-1} to 1 s^{-1}, whereas in the industrial rolling process the strain rates are much – often at least ten times – higher. This greatly affects the dynamic restoration mechanisms. However, even the dynamic restoration mechanisms, which are not likely to occur during the industrial process, must be investigated.

In EBSD measurements, cutting the sample and manual alignment of the specimen in the microscope often resulted in small deviations from the actual rolling directions, especially in the normal and transverse directions. However, the deviations from the original angles were corrected using EBSD data analysis software. If the specimen has a quite strong texture, the locations of the texture maxima are relatively easy to move to their correct locations in pole figures by turning them virtually using the software, and thereby correcting the alignment of the specimen. However, if the overall texture is weak, defining the correct locations of the intensity maxima can be very difficult and, therefore, it is possible that small errors in the alignment of the axes remain in the final data affecting the ODFs. However, the deviations are only of a couple of degrees, and therefore overall texture measurement results can be regarded as trustworthy.

In Paper II, the activation energy for hot deformation, Q_{def}, for steels containing 12–27% Cr was determined using the hyperbolic sine equation (Eq. 8). Due to the calculation method of the Q_{def} (presented in detail in Paper I), some approximations had to be carried out mainly because of three different deformation temperatures employed, and calculation of an average value based on the three temperatures. Therefore, the error in the calculations was also evaluated and presented as error bars in Fig. 9. The error bars representing the absolute error overlap, which means that the difference is not statistically significant.

The flow stress models developed in Papers I and II contained empirical equations and they are therefore only applicable for the deformation conditions and Cr contents used in the model development. The suitability of the equations outside those parameters or on other Cr contents cannot be guaranteed. The biggest issue in implementing the developed models for predicting the actual industrial rolling forces is the difference in the strain rate, which was relatively low in laboratory compression tests (0.01–1 s^{-1}). In order to employ the models in real rolling schedule planning, additional testing at higher strain rates should be carried out and the model modified based on those results.

When determining the dynamic microstructure evolution and dynamic restoration mechanisms, the specimens were water quenched as quickly as possible after the deformation pass. Due to limitations of the testing equipment, this resulted in a short delay period, and in the TMC machine the delay was about 0.4 s. However, the quench itself was very efficient in the TMC machine, whereas the water quench in Gleeble took significantly longer. In Gleeble experiments, the time for cooling the specimen from the high deformation pass temperature to room temperature was a couple of seconds even when using water quenching. Due to the delay period or inefficient quench, some further static microstructural development might have occurred and, therefore, the dynamic restoration mechanisms were postulated but it was not possible to verify them.

5.10 Recommendations for further research

The current investigations leave room for further investigations partly because some areas of hot deformation were not covered or because new questions arose when analyzing the results.

As discussed earlier, the currently developed flow stress models were both empirical, although the second one was based on Bergström's physical model. It would be a fascinating challenge to develop a flow stress model completely physical in nature and still able to incorporate the effect of Cr. Also, it would be interesting to apply other physical models, e.g. the model by Roters *et al.* [39], to the current data, and make a comparison of the applicability of various models for the high-Cr ferritic stainless steels. Furthermore, for the industrial application of these models, a set of real industrial data should be used as a basis of the flow stress model and further model development should be carried out.

Precipitation plays an important role in the hot deformation behavior of high-Cr ferritic stainless steels; however, this was discussed only in passing in Paper IV.

Deformation-induced precipitation is likely to affect the flow stress as precipitates are known to interact with dislocations during deformation and pin the moving grain and subgrain boundaries during annealing. Therefore, in order to thoroughly understand the behavior of these steels in hot deformation, investigations into precipitation behavior should be carried out. TEM characterization of the actual specimens with precipitates together with computational thermodynamic calculations, e.g. by ThermoCalc, would paint a more complete picture of the physical metallurgy and hot deformation behavior of these steels.

In the current study, no undulations or peak stress behavior were observed in the hot compression tests. It would be interesting to carry out multiple compression tests with a much greater scale of Z than in Paper III so as to investigate whether the DRV-controlled flow behavior occurs under a wider range of deformation conditions in ferritic stainless steels. It would also be interesting to carry out torsion tests, where much greater strains could be achieved, in order to investigate the flow stress development at very high strains. Microstructural investigations for specimens deformed in torsion would also bring out new information on microstructure evolution.

In Paper III, altering Z led to very different LAGB and HAGB structures, as seen in Figs. 13 and 15. The amount of substructure and number of different boundaries in the microstructure are likely to also affect the corrosion properties. However, investigations into the corrosion behavior of steels with the same compositions but with different HAGB and LAGB structures have not been carried out before.

Most importantly, it would be necessary to perform full production route simulations for the both proposed improved processing routes in order to verify their effects on the final product properties and to identify the product properties of warm rolled ferritic stainless steel hot band.

6 Summary and conclusions

The behavior of stabilized high-Cr ferritic stainless steels was investigated in hot deformation in order to determine the effect of the deformation conditions on the microstructure, texture and dislocation structure, and to develop flow stress models for ferritic stainless steels with various Cr contents. The ultimate aim of this study was to find ways to enhance the conventional hot rolling procedure in order to improve the formability, especially the deep drawability, of the end product. Hot deformation was simulated on a Gleeble 1500 thermomechanical simulator and on a TMC machine, and the microstructures were investigated by SEM-EBSD and TEM. The main results and conclusions can be summarized as follows:

- The flow curves of high-Cr ferritic stainless steel were dominated by dynamic recovery. No distinct peak stress or undulations were observed in the flow curves. A steady state was achieved under low Zener-Hollomon parameter deformation, but under high Zener-Hollomon parameter, slight work hardening was continued up to the end of the compression test.
- Cr increased the flow stress through solid solution strengthening. However, increasing the Cr content reduced the apparent activation energy for hot deformation, which decreased systemically from 359 kJ/mol to 329 kJ/mol when the Cr content increased from 12% to 27%. The reason for this phenomenon was not clear.
- Flow stress modeling was carried out successfully by using an empirical constitutive equation based on the Arrhenius equation and a set of physical-empirical equations, which are based on Bergström's physical flow stress model. The Bergström model was employed here for the first time on ferrite at high hot deformation temperatures. The effect of strain was incorporated into the parameters of the constitutive equations, and the effect of Cr on the flow stress was presented by describing two of the parameters of the Bergström's model by empirical equations.
- Static recrystallization took place after deformation at high temperatures. However, towards the completion of the process the static recrystallization kinetics slowed down more than expected from the Avrami fits. Especially the last 5–10% of the microstructure, which consisted of recovered α fiber grains, was slow to recrystallize.

- Under a low Zener-Hollomon parameter ($Z = 4.67 \times 10^{14}$ s^{-1}), continuous dynamic recrystallization took place and resulted in an abnormally large grain and subgrain size. Under medium Zener-Hollomon parameter ($Z = 4.67 \times 10^{16}$ s^{-1}, i.e. at 1050 °C and 10 s^{-1}), continuous dynamic recrystallization took place; however, the occurrence of discontinuous dynamic recrystallization was also possible. Under the highest Zener-Hollomon parameter ($Z = 8.91 \times 10^{17}$ s^{-1}), dynamic recovery and at the highest strains of 1 and 1.5, geometric dynamic recrystallization and/or continuous dynamic recrystallization took place.
- Continuous dynamic recrystallization under low Zener-Hollomon parameter did not lead to any grain refinement unlike during the deformation of ultra-fine grained materials under high Zener-Hollomon parameter. Increasing the Zener-Hollomon parameter led to a finer recrystallized grain size and sub grain size.
- Continuous dynamic recrystallization under low Zener-Hollomon parameter led to very weak γ fiber texture. However, under other deformation conditions, both α and γ texture fibers were developed. The other dynamic recrystallization mechanisms did not affect the texture formation, since the dynamically recrystallized fraction remained low.
- The dislocation structures of the deformed specimens were in accordance with the amount of dynamic recovery observed in the flow curves and the amount of low angle grain boundaries in the microstructure investigations. The density of dislocations was highest under deformation at the highest Zener-Hollomon parameters, and the dislocations were mainly in numerous dislocation tangles. Under the lowest Zener-Hollomon parameters, the dislocation structures were recovered and cells and subgrains had formed.
- Lowering the hot deformation temperature increased the number of low angle grain boundaries, and at 800 °C or below in-grain shear bands were formed in the grains belonging to the γ fiber.
- At 1 s^{-1}, lowering the deformation temperature to 600 °C or below led to a shift in the location of the texture intensity maxima along the α fiber and formation of strong γ fiber during recrystallization annealing. However, during deformation at 20 s^{-1} the deformation temperature did not affect the locations of the intensity maxima.
- Lowering the deformation temperature to 800 and 750 °C accelerated the static recrystallization kinetics, but did not lead to a favorable texture

development during annealing, most probably as a result of the remaining unrecrystallized grains, which belonged to the α fiber.

- During simulated industrial Steckel mill rolling, the material underwent complete softening during the inter-pass periods. However, static recrystallization was unlikely to be fully completed, but the effective static recovery ensured the softening.
- In conventional hot rolling of ferritic stainless steels, any form of dynamic recrystallization is unlikely due to a lack of sufficient dislocation accumulation, which is caused by intense dynamic recovery.
- Two improved hot and warm rolling routes were proposed, which should lead to improved final product properties.
- In the first proposed route, the hot rolling finishing temperature is lowered in order to increase the amount of stored energy in the microstructure and to induce the formation of in-grain shear bands during the final rolling passes. It is assumed that, by taking these measures, static recrystallization is enhanced during hot band annealing and nucleation of static recrystallization in the in-grain shear bands, the amount of γ fiber texture should be increased, which would lead to enhancement of the final product properties.
- The second proposed method is carrying out heavy warm rolling, in which all of the hot rolling passes are carried out at a lower temperature, i.e. at 800 °C with shorter inter-pass times so as to allow dislocation accumulation and continuous and geometric dynamic recrystallization, which would reduce the grain size already during the deformation passes. Combining heavy warm rolling with hot band annealing, it would be possible to produce thin gauge hot band with a fine grain size and strong γ fiber texture, and therefore presumably also good deep drawability.

7 Novel features

The following methods and findings are believed to be original:

- Application of Bergström's model for predicting hot deformation flow stress curves of ferritic stainless steels.
- Development of a flow stress model, which incorporates the effect of Cr into the equations for ferritic stainless steels.
- Effect of dynamic restoration mechanisms on texture development in plane strain deformation for ferritic steel. Disappearance of the γ fiber when continuous dynamic recovery occurred under low Zener-Hollomon parameter deformation conditions.
- Continuous dynamic recrystallization, when occurring under low Zener-Hollomon parameter conditions, does not lead to grain refinement as it would under high Zener-Hollomon parameter deformation, according to the literature.
- Reporting the microstructure and texture development of stabilized high-Cr ferritic stainless steels during simulated multi-pass hot rolling.
- Specifying the temperature range that would lead to both improved texture structure and static recrystallization kinetics during hot band annealing. Lowering the temperature to 800 °C and 750 °C increased the static recrystallization kinetics, but had no positive effect on texture development. The positive effect on the texture development was achieved when lowering the deformation temperature to 600 °C or below.

References

1. Yazawa Y, Ishii K, Ishii T, Okada S, Ujiro T & Yamasita H (2007) JFE443CT, Ni Mo-Free Stainless Steel with High Corrosion Resistance. Corrosion Engineering 56(10): 599–606.
2. Shin H-J, An J-K, Park SH & Lee DN (2003) The effect of texture on ridging of ferritic stainless steel. Acta Mater 51(16): 4693–4706.
3. Yazawa Y, Ozaki Y, Kato Y & Furukimi O (2003) Development of ferritic stainless steel sheets with excellent deep drawability by {111} recrystallization texture control. JSAE Review 24(4): 483–488.
4. Yazawa Y, Muraki M, Kato Y & Furukimi O (2003) Effect of Chromium Content on Relationship Between r-value and {111} Recrystallization Texture in Ferritic Steel. ISIJ Int 43(10): 1647–1651.
5. Huh M-Y & Engler O (2001) Effect of intermediate annealing on texture, formability and ridging of 17%Cr ferritic stainless steel sheet. Mater Sci Eng A 308(1–2): 74–87.
6. Park SH, Kim KY, Lee YD & Park CG (2002) Evolution of microstructure and texture associated with ridging in ferritic stainless steels. ISIJ Int 42(1): 100–105.
7. Raabe D (1995) Experimental investigation and simulation of crystallographic rolling textures of Fe–11Cr steel. Mater Sci Tech 11(10): 985–993.
8. Raabe D & Lucke K (1992) Influence of particles on recrystallization textures of ferritic stainless steels. Steel Res 63(10): 457–464.
9. Sinclair CW & Mithieux J-D (2004) Coupling recrystallization and texture to the mechanical properties of ferritic stainless steel sheet. Mater Sci Forum 467–470(I): 317–322.
10. Glover G & Sellars CM (1972) Static recrystallization after hot deformation of α-iron. Metall Trans 3(8): 2271–2280.
11. Glover G & Sellars CM (1973) Recovery and recrystallization during high temperature deformation of α-iron. Metall Trans 4(3): 765–775.
12. Hinton JS & Beynon JH (2007) Restoration processes during hot deformation in the δ-ferrite and austenite dual phase region of AlS1430 ferritic stainless steel. ISIJ Int 47(10): 1465–1474.
13. Gao F, Liu Z, Liu H & Wang G (2011) Influence of the finish rolling temperatures on the microstructure and texture evolution in the ferritic stainless steels. Acta Metallurgica Sinica (English Letters) 24(5): 343–350.
14. Gao F, Liu Z, Liu H & Wang G (2012) Texture evolution and formability under different hot rolling conditions in ultrapurified 17%Cr ferritic stainless steels. Mater Charact 75: 93–100.
15. Zhang C, Liu Z & Wang G (2011) Effects of hot rolled shear bands on formability and surface ridging of an ultrapurified 21%Cr ferritic stainless steel. J Mater Process Tech 211(6): 1051–1059.
16. Gao F, Yourong XU, Song B & Xia K (2000) Substructural changes during hot deformation of an Fe-26Cr ferritic stainless steel. Metall Mat Trans A 31A(1): 21–27.

17. Sinclair CW, Mithieux J-D, Schmitt J-H & Brechet Y (2005) Recrystallization of stabilized ferritic stainless steel sheet. Metall Mater Trans A 36A(11): 3205–3215.
18. Sinclair CW, Weygand D, Lepinoux J & Brechet Y (2004) Simulating the topology of recrystallization in stabilized ferritic stainless steels. Mater Sci Forum 467-470: 671–676.
19. Sinclair CW, Robaut F, Maniguet L, Mithieux J-D, Schmitt J-D & Brechet Y (2003) Recrystallization and texture in a ferritic stainless steel: an EBSD study. Advanced Engineering Materials 5(8): 570–574.
20. Barnett MR (1998) Role of in-grain shear bands in the nucleation of <111>//ND recrystallization textures in warm rolled steel. ISIJ Int 38(1): 78–85.
21. Barnett MR & Jonas JJ (1997) Influence of ferrite rolling temperature on microstructure and texture in deformed low C and IF steels. ISIJ Int 37(7): 697–705.
22. Barnett MR & Jonas JJ (1997) Influence of ferrite rolling temperature on grain size and texture in annealed low C and IF steels. ISIJ Int 37(7): 706–714.
23. Jonas JJ (2001) Effects of shear band formation on texture development in warm-rolled IF steels. J Mater Process Tech 117(3): 293–299.
24. Liu D, Humphreys AO, Toroghinejad MR & Jonas JJ (2002) The deformation microstructure and recrystallization behavior of warm rolled steels. ISIJ Int 42(7): 751–758.
25. Toroghinejad MR, Humphreys AO, Liu D, Ashrafizadeh F, Najafizadeh A & Jonas JJ (2003) Effect of rolling temperature on the deformation and recrystallization textures of warm-rolled steels. Metall Mat Trans A 34 A(5): 1163–1174.
26. Frost HJ & Ashby MF (1982) Deformation-mechanism maps: the plasticity and creep of metals and ceramics. Oxford, Pergamon Press.
27. Honeycombe RWK (1984) Plastic deformation of metals. London, Edward Arnold.
28. Sellars CM & Tegart WJ (1966) La relation entre la resistance et la structure dans la deformation a chaud. Mem Sci Rev Met 63: 731–46.
29. McQueen HJ & Imbert CAC (2004) Dynamic recrystallization: plasticity enhancing structural development. J Alloy Compd 378(1–2): 35–43.
30. McQueen HJ & Ryan ND (2002) Constitutive analysis in hot working. Mater Sci Eng A 322(1–2): 43–63.
31. Sellars CM & McTegart WJ (1966) On the mechanism of hot deformation. Acta Metall 14(9): 1136–1138.
32. McQueen HJ (1968) Deformation mechanisms in hot working. Journal of Metals 20(4): 31–38.
33. Briottet L, Jonas JJ & Montheillet F (1996) A mechanical interpretation of the activation energy of high temperature deformation in two phase materials. Acta Mater 44(4): 1665–1672.
34. Laasraoui A & Jonas JJ (1991) Prediction of steel flow stresses at high temperatures and strain rates. Metall Trans A 22(7): 1545–1558.
35. Zener C & Hollomon JH (1944) Effect of strain rate upon plastic flow of steel. J Appl Phys 15(1): 22–32.

36. Bergström Y & Aronsson B (1972) The application of a dislocation model to the strain and temperature dependence of the strain hardening exponent n in the Ludwik-Hollomon relation between stress and strain in mild steels. Metall Trans 3(7): 1951–1957.
37. Roberts W & Bergström Y (1973) The stress-strain behaviour of single crystals and polycrystals of face-centered cubic metals-a new dislocation treatment. Acta Metall 21(4): 457–469.
38. Bergström Y (1982) The plastic deformation of metals - A dislocation model and its applicability. PhD thesis. Stockholm, Royal Institute of Technology.
39. Roters F, Raabe D & Gottstein G (2000) Work hardening in heterogeneous alloys - a microstructural approach based on three internal state variables. Acta Mater 48(17): 4181–4189.
40. Rao KP & Prasad YKDV (1995) Neural network approach to flow stress evaluation in hot deformation. J Mater Process Tech 53(3–4): 552–566.
41. Lin YC, Zhang J & Zhong J (2008) Application of neural networks to predict the elevated temperature flow behavior of a low alloy steel. Comp Mater Sci 43(4): 752–758.
42. Phaniraj MP & Lahiri AK (2003) The applicability of neural network model to predict flow stress for carbon steels. J Mater Process Tech 141(2): 219–227.
43. Bergström Y (1970) A dislocation model for the stress-strain behaviour of polycrystalline α-Fe with special emphasis on the variation of the densities of mobile and immobile dislocations (abstract). Mater Sci Eng 5(4): 193–200.
44. Humphreys FJ & Hatherly M (1995) Recrystallization and related annealing phenomena. Oxford, Pergamon.
45. Desrayaud C, Girard S, Le Coze J & Montheillet F (2002) Influence of carbon additions on the dynamic recrystallization of high purity α-iron. Materials Transactions 43(2): 135–140.
46. Longfei L, Wangyue Y & Zuqing S (2006) Dynamic recrystallization of ferrite in a low-carbon steel. Metall Mat Trans A 37(3): 609–619.
47. McQueen HJ (2004) Development of dynamic recrystallization theory. Mater Sci Eng A 387–389: 203–208.
48. Luton MJ & Sellars CM (1969) Dynamic recrystallization in nickel and nickel-iron alloys during high temperature deformation. Acta Metall 17(8): 1033–1043.
49. Sakai T & Jonas JJ (1984) Overview no. 35 Dynamic recrystallization: Mechanical and microstructural considerations. Acta Metall 32(2): 189–209.
50. Yamagata H, Ohuchida Y, Saito N & Otsuka M (2001) Nucleation of new grains during discontinuous dynamic recrystallization of 99.998 mass% aluminum at 453 K. Scr Mater 45(9): 1055–1061.
51. Yamagata H (1995) Dynamic recrystallization and dynamic recovery in pure aluminum at 583K. Acta Metall Mater 43(2): 723–729.
52. Ponge D, Bredehöft M & Gottstein G (1997) Dynamic recrystallization in high purity aluminum. Scr Mater 37(11): 1769–1775.

53. Tsuji N, Matsubara Y & Saito Y (1997) Dynamic recrystallization of ferrite in interstitial free steel. Scr Mater 37(4): 477–484.
54. McQueen HJ & Kassner ME (2004) Comments on a model of continuous dynamic recrystallization proposed for aluminum. Scr Mater 51(5): 461–465.
55. Kassner ME & Barrabes SR (2005) New developments in geometric dynamic recrystallization. Mater Sci Eng A 410–411: 152–155.
56. Henshall GA, Kassner ME & McQueen HJ (1992) Dynamic restoration mechanisms in Al-5.8 At. Pct Mg deformed to large strains in the solute drag regime. Metall Trans A 23(3): 881–889.
57. Blum W, Zhu Q, Merkel R & McQueen HJ (1996) Geometric dynamic recrystallization in hot torsion of Al-5Mg-0.6Mn (AA5083). Mater Sci Eng A 205(1–2): 23–30.
58. Poletti C, Rodriguez-Hortalá M, Hauser M & Sommitsch C (2011) Microstructure development in hot deformed AA6082. Mater Sci Eng A 528(6): 2423–2430.
59. Gourdet S & Montheillet F (2003) A model of continuous dynamic recrystallization. Acta Mater 51(9): 2685–2699.
60. McQueen HJ & Blum W (2000) Dynamic recovery: sufficient mechanism in the hot deformation of Al (< 99.99). Mater Sci Eng A 290(1–2): 95–107.
61. Montheillet F & Gourdet S (2000) An experimental study of the recrystallization mechanism during hot deformation of aluminium. Mater Sci Eng A 283(1–2): 274–288.
62. Dougherty LM, Robertson IM & Vetrano JS (2003) Direct observation of the behavior of grain boundaries during continuous dynamic recrystallization in an Al-4Mg-0.3Sc alloy. Acta Mater 51(15): 4367–4378.
63. Hu HE, Zhen L, Zhang BY, Yang L & Chen JZ (2008) Microstructure characterization of 7050 aluminum alloy during dynamic recrystallization and dynamic recovery. Mater Charact 59(9): 1185–1189.
64. Oliveira TR & Montheillet F (2004) Effect of Niobium and titanium on the dynamic recrystallization during hot deformation of stabilized ferritic stainless steels. Mater Sci Forum 467–470: 1229–1236.
65. Kim S & Yoo Y (2002) Continuous dynamic recrystallization of AISI 430 ferritic stainless steel. Metals and Materials Int 8(1): 7–13.
66. Oudin A, Hodgson PD & Barnett MR (2008) EBSD analysis of a Ti-IF steel subjected to hot torsion in the ferritic region. Mater Sci Eng A 486(1–2): 72–79.
67. Eghbali B, Abdollah-Zadeh A, Beladi H & Hodgson PD (2006) Characterization on ferrite microstructure evolution during large strain warm torsion testing of plain low carbon steel. Mater Sci Eng A 435–436: 499–503.
68. Eghbali B, Abdollah-Zadeh A & Hodgson PD (2007) Dynamic softening of ferrite during large strain warm deformation of a plain-carbon steel. Mater Sci Eng A 462(1–2): 259–263.
69. Eghbali B (2010) Effect of strain rate on the microstructural development through continuous dynamic recrystallization in a microalloyed steel. Mater Sci Eng A 527(15): 3402–3406.

70. Narayana Murty SVS, Torizuka S, Nagai K, Koseki N & Kogo Y (2005) Classification of microstructural evolution during large strain high Z deformation of a 0.15 carbon steel. Scr Mater 52(8): 713–718.
71. Narayana Murty SVS, Torizuka S, Nagai K, Kitai T & Kogo Y (2005) Dynamic recrystallization of ferrite during warm deformation of ultrafine grained ultra-low carbon steel. Scr Mater 53(6): 763–768.
72. Sakai T, Belyakov A & Miura H (2008) Ultrafine Grain Formation in Ferritic Stainless Steel during Severe Plastic Deformation. Metall Mater Trans A 39(9): 2206–2214.
73. Belyakov A, Kaibyshev R & Sakai T (1998) New grain formation during warm deformation of ferritic stainless steel. Metall Mat Trans A 29(1): 161–167.
74. Avrami M (1939) Kinetics of phase change. I: General theory. J Chem Phys 7(12): 1103–1112.
75. Laasraoui A & Jonas JJ (1991) Recrystallization of austenite after deformation at high temperatures and strain rates - analysis and modeling. Metall Trans A 22A(1): 151–160.
76. Sellars CM & Whiteman JA (1978) Recrystallization and grain growth in hot rolling. Met Sci 13(3–4): 187–194.
77. Tsuji N, Shinmiya T, Saito Y & Muraki M (1998) Deformation Microstructure and Nucleation of Recrystallization in Hot-deformed Single Crystals of 18% Cr Ferritic Steel. ISIJ Int 38(4): 380–389.
78. Tsuji N, Tsuzaki K & Maki T (1993) Effect of initial orientation on the recrystallization behavior of solidified columnar crystals in a 19% Cr ferritic stainless steel. ISIJ Int 33(7): 783–792.
79. Tsuji N, Tsuzaki K & Maki T (1994) Effects of rolling reduction and annealing temperature on the recrystallization structure of solidified columnar crystals in a 19% Cr ferritic stainless steel. ISIJ Int 34(12): 1008–1017.
80. Raabe D & Lucke K (1993) Textures of ferritic stainless steels. Mater Sci Tech 9(4): 302–312.
81. Lücke K & Hölscher M (1991) Rolling and recrystallization textures of BCC steels. Textures and Microstructures 14–18: 585–596.
82. Yan H, Bi H, Li X & Xu Z (2009) Microstructure, texture and grain boundaries character distribution evolution of ferritic stainless steel during rolling process. J Mater Process Tech 209(5): 2627–2631.
83. Holscher M, Raabe D & Lucke K (1991) Rolling and Recrystallization Textures of BCC Steels. Steel Res 62(12): 567–575.
84. Akbari GH, Sellars CM & Whiteman JA (1997) Microstructural development during warm rolling of an IF steel. Acta Mater 45(12): 5047–5058.
85. Khatirkar R, Kestens LAI, Petrov R & Samajdar I (2009) Controlled warm working: Possible tool for optimizing stored energy advantage in deformed γ-fiber (ND//<111>). ISIJ Int 49(1): 78–85.

86. Haldar A, Huang X, Leffers T, Hansen N & Ray RK (2004) Grain orientation dependence of microstructures in a warm rolled IF steel. Acta Mater 52(18): 5405–5418.
87. Huh M-Y, Lee J-H, Park SH, Engler O & Raabe D (2005) Effect of through-thickness macro and micro-texture gradients on ridging of 17%Cr ferritic stainless steel sheet. Steel Res Int 76(11): 797–806.
88. Matsuoka S, Sakata K, Satoh S & Kato T (1994) Effect of hot-rolCg strain rate in the ferrite region on the recrystallization texture of extra-low C sheet steels. ISIJ Int 34(1): 77–84.
89. Lee YD, Ryoo DY, Lee YY & Park SH (1990) Recrystallization Behaviours of Low Carbon Ferritic Stainless Steels During Hot Rolling and Annealing Process. In: Proceedings of Recrystallization '90. Wollongong, Australia: 435–440.
90. Sawatani T, Shimizu K, Nakayama T & Miyoshi M (1978) The r-Values and Recrystallized Textures of Ti-Stabilized Low C, N-17%Cr Stainless Steel Sheets. Trans Iron Steel Inst Jpn 18(11): 676–685.
91. Slooff FA, Zhou J, Duszczyk J & Katgerman L (2007) Constitutive analysis of wrought magnesium alloy Mg-Al4-Zn1. Scr Mater 57(8): 759–762.
92. Lin Y-C, Chen M-S & Zhang J (2009) Modeling of flow stress of 42CrMo steel under hot compression. Mater Sci Eng A 499(1–2): 88–92.
93. Samantaray D, Phaniraj C, Mandal S & Bhaduri AK (2011) Strain dependent rate equation to predict elevated temperature flow behavior of modified 9Cr-1Mo (P91) steel. Mater Sci Eng A 528(3): 1071–1077.
94. Mirzadeh H, Cabrera JM & Najafizadeh A (2012) Modeling and prediction of hot deformation flow curves. Metall Mat Trans A 43(1): 108–123.
95. Shewmon P (1989) Diffusion in solids. Warrendale, TMS.
96. Lin YC, Chen M-S & Zhong J (2008) Constitutive modeling for elevated temperature flow behavior of 42CrMo steel. Comput Mater Sci 42(3): 470–477.
97. Mandal S, Rakesh V, Sivaprasad PV, Venugopal S &, Kasiviswanathan KV (2009) Constitutive equations to predict high temperature flow stress in a Ti-modified austenitic stainless steel. Mater Sci Eng A 500(1–2): 114–121.
98. Loveday MS, Mahon GJ, Roebuck B, Lacey AJ, Palmiere EJ, Sellars CM, van den Winden MR (2006) Measurement of flow stress in hot plane strain compression tests. Mater High Temp 23(2): 85–118.
99. Gao F, Liu Z-Y & Wang G-D (2011) Hot deformation behavior of high-purified 17%Cr ferritic stainless steel (abstract). Dongbei Daxue Xuebao/Journal of Northeastern University 32(10): 1406–1409.
100. Oudin A, Barnett MR & Hodgson PD (2004) Grain size effect on the warm deformation behavior of a Ti-IF steel. Mater Sci Eng A 367: 282–294.
101. Sun D, Li M, Zou Y, Yang R & Li F (1997) A model for dynamic recovery of bcc structure. Chinese Science Bulletin 42(14): 1211–1215.
102. Medina SF & Hernandez CA (1996) General expression of the Zener-Hollomon parameter as a function of the chemical composition of low alloy and microalloyed steels. Acta Mater 44(1): 137–48.

103. Somani MC & Karjalainen LP (2007) Modeling the deformation and annealing processes: Physical and regression approaches. Mater Sci Forum 550: 583–588.
104. Serajzadeh S & Taheri AK (2002) An investigation on the effect of carbon and silicon on flow behavior of steel. Mater Des 23(3): 271–276.
105. Bergström Y, Granbom Y & Sterkenburg D (2010) A dislocation-based theory for the deformation hardening behavior of DP steels: Impact of martensite content and ferrite grain size. Journal of Metallurgy Article ID 647198. URL: http://www.hindawi.com/journals/jm/2010/647198/. Cited 2013/12/2.
106. Qin Y-J, Pan Q-L, He Y-B, Li W-B, Liu X-Y & Fan X (2010) Modeling of flow stress for magnesium alloy during hot deformation. Mater Sci Eng A 527(10–11): 2790–2797.
107. Najafi-Zadeh A, Jonas JJ & Yue S (1992) Grain refinement by dynamic recrystallization during the simulated warm-rolling of interstitial free steels. Metall Trans A 23(9): 2607–2617.
108. Barraclough DR & Sellars CM (1979) Static recrystallization and restoration after hot deformation of type 304 stainless steel. Met Sci 13(3–4): 257–268.
109. Karjalainen JP, Koskiniemi JA & Liu XD (1996) Static recrystallization in austenitic and ferritic stainless steels investigated by the stress relaxation method. In: Proceedings of 37th MNWSP Conference, Hamilton, Canada: 861–869.
110. Akbari GH, Sellars CM & Whiteman JA (2002) Static restoration processes in warm rolled interstitial free steel. Mater Sci Technol 18: 885–891.
111. Belyakov A, Tsuzaki K & Kimura Y (2008) Regularities of deformation microstructures in ferritic stainless steels during large strain cold working. ISIJ Int 48(8): 1071–1079.
112. Zhao H, Rama SC, Barber GC, Wang Z & Wang X (2002) Experimental study of deep drawability of hot rolled IF steel. J Mater Process Tech 128(1-3): 73–79.
113. Tomitz A & Kaspar R (2000) Deep-drawable thin-gauge hot strip of steel as a substitution for cold strip. ISIJ Int 40(9): 927–931.
114. Zambrano PC, Delgado AL, Guerrero-Mata MP, Colás R & Leduc LA (2003) Hot rolling of light gauge steel strip. ISIJ Int 43(7): 1030–1035.
115. Petrov R, Kestens L, Zambrano PC, Guerrero MP, Colás R & Houbaert Y (2003) Microtexture of thin gauge hot rolled steel strip. ISIJ Int 43(3): 378–385.

Original publications

I Mehtonen S, Karjalainen P & Porter D (2014) Modeling of the high temperature flow behavior of stabilized 12–27 wt% Cr ferritic stainless steels. Materials Science & Engineering A 607: 44–52.

II Mehtonen S, Karjalainen P & Porter D (2013) Hot deformation behavior and microstructure evolution of a stabilized high-Cr ferritic stainless steel. Materials Science & Engineering A 571: 1–12.

III Mehtonen S, Palmiere E, Misra D, Karjalainen P & Porter D (2014) Dynamic restoration mechanisms in a Ti-Nb stabilized ferritic stainless steel during hot deformation. Materials Science & Engineering A 601: 7–19.

IV Mehtonen S, Palmiere E, Misra D, Karjalainen P & Porter D (2014) Microstructural and texture development during multi-pass hot deformation of a stabilized high-chromium ferritic stainless steel. ISIJ International 54(6): 1406–1415.

V Mehtonen S, Karjalainen P & Porter D (2013) Effect of hot deformation temperature on the restoration mechanisms and texture in a high-Cr ferritic stainless steel. Materials Science Forum 762: 705–710.

Original publications are not included in the electronic version of the dissertation.

476. Juuso, Esko (2013) Integration of intelligent systems in development of smart adaptive systems : linguistic equation approach

477. Lu, Xiaojia (2013) Resource allocation in uplink coordinated multicell MIMO-OFDM systems with 3D channel models

478. Jung, Sang-Joong (2013) Personal machine-to-machine (M2M) healthcare system with mobile device in global networks

479. Haho, Päivi (2014) Learning enablers, learning outcomes, learning paths, and their relationships in organizational learning and change

480. Ukkonen, Kaisa (2014) Improvement of recombinant protein production in shaken cultures : focus on aeration and enzyme-controlled glucose feeding

481. Peschl, Michael (2014) An architecture for flexible manufacturing systems based on task-driven agents

482. Kangas, Jani (2014) Separation process modelling : highlighting the predictive capabilities of the models and the robustness of the solving strategies

483. Kemppainen, Kalle (2014) Towards simplified deinking systems : a study of the effects of ageing, pre-wetting and alternative pulping strategy on ink behaviour in pulping

484. Mäklin, Jani (2014) Electrical and thermal applications of carbon nanotube films

485. Niemistö, Johanna (2014) Towards sustainable and efficient biofuels production : use of pervaporation in product recovery and purification

486. Liu, Meirong (2014) Efficient super-peer-based coordinated service provision

487. Väyrynen, Eero (2014) Emotion recognition from speech using prosodic features

488. Celentano, Ulrico (2014) Dependable cognitive wireless networking : modelling and design

489. Peräntie, Jani (2014) Electric-field-induced dielectric and caloric effects in relaxor ferroelectrics

490. Aapaoja, Aki (2014) Enhancing value creation of construction projects through early stakeholder involvement and integration

491. Rossi, Pekka M. (2014) Integrated management of groundwater and dependent ecosystems in a Finnish esker

492. Sliz, Rafal (2014) Analysis of wetting and optical properties of materials developed for novel printed solar cells

Book orders:
Granum: Virtual book store
http://granum.uta.fi/granum/

UNIVERSITY OF OULU P.O. Box 8000 FI-90014 UNIVERSITY OF OULU FINLAND

ACTA UNIVERSITATIS OULUENSIS

ISBN 978-952-62-0493-2 (Paperback)
ISBN 978-952-62-0494-9 (PDF)
ISSN 0355-3213 (Print)
ISSN 1796-2226 (Online)

UNIVERSITY of OULU
OULUN YLIOPISTO